Article:

Sharifian, M.K., Kesserwani, G. and Hassanzadeh, Y. (2018) A discontinuous Galerkin approach for conservative modelling of fully nonlinear and weakly dispersive wave transformations. Ocean Modelling, 125. pp. 61-79. ISSN 1463-5003

https://doi.org/10.1016/j.ocemod.2018.03.006

A discontinuous Galerkin approach for conservative modelling of fully nonlinear and weakly dispersive wave transformations

Mohammad Kazem Sharifian[a,*], Georges Kesserwani[b], Yousef Hassanzadeh[a]

[a] Department of Civil Engineering, University of Tabriz, Tabriz, Iran

[b] Department of Civil and Structural Engineering, University of Sheffield, Sheffield S1 3JD, UK

Abstract

This work extends a robust second-order Runge-Kutta Discontinuous Galerkin (RKDG2) method to solve the fully nonlinear and weakly dispersive flows, within a scope to simultaneously address accuracy, conservativeness, cost-efficiency and practical needs. The mathematical model governing such flows is based on a variant form of the Green-Naghdi (GN) equations decomposed as a hyperbolic shallow water system with an elliptic source term. Practical features of relevance (i.e. conservative modelling over irregular terrain with wetting and drying and local slope limiting) have been restored from an RKDG2 solver to the Nonlinear Shallow Water (NSW) equations, alongside new considerations to integrate elliptic source terms (i.e. via a fourth-order local discretization of the topography) and to enable local capturing of breaking waves (i.e. via adding a detector for switching off the dispersive terms). Numerical results are presented, demonstrating the overall capability of the proposed approach in achieving realistic prediction of nearshore wave processes involving both nonlinearity and dispersion effects within a single model.

*Corresponding author:
E-mail addresses: m.sharifian@tabrizu.ac.ir (M.K. Sharifian); g.kesserwani@sheffield.ac.uk (G. Kesserwani); yhassanzadeh@tabrizu.ac.ir (Y. Hassanzadeh)

1- Introduction

The last decades have seen significant advances in the development of numerical models for coastal engineering applications, which have the ability to accurately represent waves traveling from deep water into the shoreline (Kirby, 2016). Such models should account for nonlinear phenomena resulting from wave interaction with structures, and dispersive phenomena due to the wave propagation over a wide range of depths (Walkley, 1999). Various simplifications of the Navier-Stokes equations (Ma et al., 2012) have been proposed to enable affordable modelling of water wave problems. Most commonly, researchers have relied on the depth-integrated Nonlinear Shallow Water (NSW) equations, which seems to work well for shallow flow modelling but are specifically not ideal for coastal applications involving deeper water and wave shoaling (Brocchini and Dodd, 2008; Brocchini, 2013).

As an alternative, Boussinesq-type (BT) equations introduce dispersion terms and are more suitable in water regions where dispersion begins to have an effect on the free surface. These models represent the depth-integrated expressions of conservation of mass and momentum for weakly nonlinear and weakly dispersive waves, where the vertical profile of velocity potential is parabolic. Peregrine (1967) used Taylor expansion of the vertical velocity about a specific level and extended the NSW equations asymptotically into deeper water. Since the pioneering work of Peregrine (1967), the Boussinesq theory has experienced many developments in accuracy, and in extension of the range of application beyond the weakly nonlinear and weakly dispersive assumptions, which were confined to relatively shallow waters (Madsen et al., 1991; Madsen and Sørensen, 1992; Nwogu, 1993; Wei et al., 1995; Schäffer and Madsen, 1995; Beji and Nadaoka, 1996; Madsen and Schäffer, 1998; Agnon et al., 1999; Gobbi et al., 2000; Madsen et al., 2002, 2003; Lynett and Liu, 2004a, 2004b). However, most of the enhanced BT models remain not entirely nonlinear and bring about complexities associated with the involvement of high order derivatives. It also should be noted that the Non-Hydrostatic Shallow Water (NHSW) models are another class of equations which have gained attention recently (Zijlema and Stelling, 2008; Yamazaki et al., 2009; Bai and Cheung, 2013; Wei and Jia, 2013; Lu et al., 2015). These models could be seen as a variant of BT models with alternative approaches to model fully nonlinear and weakly dispersive waves (Kirby, 2016).

The so-called Green-Naghdi (GN) equations (Green and Naghdi, 1976), also known as Serre equations (Serre, 1953), are viewed as fully nonlinear and weakly dispersive BT equations in which there is no restriction on the order of magnitude of nonlinearity, thereby providing the capability to describe large amplitude wave propagation in shallow waters. These equations were first derived by Serre (1953); several years later, they were re-derived by Green and Naghdi (1976) using a different method. A 1D formal derivation of these equations can be found in Barthélemy (2004) for flat bottoms and in Cienfuegos et al. (2006) for non-flat bottoms. Alvarez-Samaniego and Lannes (2008) showed that GN models can accurately predict the important characteristics of the waves in comparison with the Euler equations. Israwi (2010) derived a new 2D version of the GN system that possesses the capability of accounting for the horizontal vorticity. More recently, Bonneton et al. (2011) and Lannes and Marche (2015) derived a new system that is asymptotically equal to the classic GN equations but is featured with a much simpler structure, which is easier to be solved numerically.

From a numerical modelling viewpoint, various approaches have been used for solving BT equations considering Finite Difference (FD) methods (Wei and Kirby, 1995), Finite Element (FE) methods (Filippini et al., 2016), Finite Volume (FV) methods (Cienfuegos et al., 2006; Le Métayer et al., 2010; Dutykh et al., 2011) and hybrid FV/FD approaches (Bonneton et al., 2011; Orszaghova et al., 2012; Tissier et al., 2012), to cite a few.

The FV discretization seems to be the most widely adopted among the other approaches used for the numerical approximation of both NSW and BT equations given its conservation properties, geometrical flexibility, conceptually simple basis, and ease of implementation. Nonetheless, the Discontinuous Galerkin (DG) discretization seems to be a promising alternative owed to its faster convergence rates and better quality predictions on coarse meshes as compared to an equally accurate FV approach (e.g. Zhou et al., 2001; Zhang and Shu, 2005; Kesserwani, 2013; Kesserwani and Wang, 2014).

For solving convection-dominated problems, a spatial DG discretization is often realized within an explicit multi-stage Runge-Kutta (RK) time stepping mechanism, leading to the standard RKDG method proposed by Cockburn and Shu (1991). A local RKDG formulation can be seen as a higher-order extension to the conservative FV method, in the Godunov (1959) sense, where one averaged variable of state over a computational element is evolved by inter-elemental local flux balance incorporating the Riemann problem solutions (Toro and Garcia-Navarro, 2007). In the RKDG method, this same principle applies, however to evolve a series of coefficients (i.e. the average and slope coefficients spanning the polynomial solution) by means of local spatial operators translated from the conservative model equations (in the weak sense). The number of coefficients that should be involved and the number of inner RK stages required are proportional to the desired order-of-accuracy; the latter is, on the other hand, inversely proportional to the maximum allowable CFL number. Hence, increase in operational and runtime costs is inevitable in line with increasing order-of-accuracy. For solving the NSW equations, many RKDG formulations were proposed (Kesserwani and Liang, 2010, 2012; Xing, 2014; Tavelli and Dumbser, 2014; Gassner et al., 2016). However, practically speaking, higher than second-order accurate RKDG (RKDG2) formulations remain significantly harder to generally stabilize, e.g. when it comes to carefully selecting and limiting slope coefficients and ensuring well-balanced and conservative numerical predictions over rough and uneven terrain (Kesserwani and Liang, 2011, 2012; Caviedes-Voullième and Kesserwani, 2015).

In the context of numerically solving elliptic equations with higher order derivatives, often the so-called Local Discontinuous Galerkin (LDG) method is employed as proposed in Cockburn and Shu (1998). Since the early 2000s, different variants of the DG method were utilized for solving the BT equations (e.g. Eskilsson and Sherwin (2003, 2005, 2006), Eskilsson et al. (2006), Engsig-Karup et al. (2006, 2008), de Brye et al. (2013); Dumbser and Facchini (2016) for enhanced Boussinesq equations; Li et al. (2014), Dong and Li (2016), and Duran and Marche (2015, 2017) for the GN equations). Most of these works lacked a full consideration and assessment to the issues of practical relevance, such as the simultaneous presence of highly irregular bathymetry, wetting and drying and friction effects. To the best of our knowledge, only the work of Duran and Marche (2015, 2017) considered some of these issues in an alternative RKDG formulation solving the GN equations derived by Lannes and Marche (2015). The investigators successfully solved the pre-balanced NSW equations with higher than second-order RKDG methods. However, the use of the pre-balanced NSW equations is unnecessary (Lu and Xie, 2016) and entails sophisticated flux terms with topography, which add on to the operational costs.

Another important practical issue in modeling nearshore wave processes is wave breaking. Like other BT models, the GN equations only provide satisfactory description of the waves up to the breaking point and cannot represent the energy dissipation pertinent to this phenomenon. To address this issue, a strategy for handling potential breaking waves must be deployed and several methods have been proposed for this purpose. One traditional method would be to add an ad-hoc viscous term to the momentum equation to account for energy dissipation (Zelt, 1991; Karambas and Koutitas, 1992; Sørensen et al., 1998; Kennedy et al., 2000; Chen et al., 2000; Cienfuegos et al., 2009; Roeber et al., 2010). Another method, which has been gaining popularity in recent years, is to simply neglect the dispersive terms so that to enable the BT model to switch to the NSW equations in the region where wave breaking takes place (e.g. Borthwick et al., 2006; Bonneton, 2007; Tonelli and Petti, 2009, 2010; Roeber and Cheung, 2012; Tissier et al., 2012; Orszaghova et al., 2012; Shi et al., 2012; Kazolea and Delis, 2013); in other words, treat the broken waves as shocks (Filippini et al., 2016). To do so, a sensor is required for triggering the initiation and possibly termination of breaking process, many of which are reported based on different physical criteria. For example, Kennedy et al. (2000) used vertical speed of the free surface elevation, Tonelli et al. (2009, 2010) employed the ratio of the surface elevation to the water depth, Roeber and Cheung (2012) involved local momentum gradients, Tissier et al., (2012) combined local energy dissipation, front slope and Froude number, and Filippini et al. (2016) combined the surface variation and local slope angle.

To this end, this paper aims to develop a robust RKDG2-based model for simulation of wave propagation from intermediate to shallow waters and its possible transformations including wave breaking. A simplified form of the GN equations (Lannes and Marche, 2015) will be considered, in which the model equations can be decomposed into the conservative form of the NSW equations and elliptic source terms accounting for dispersion effects. This decomposition will be exploited to enable handling breaking waves by switching off the dispersive terms based on an entirely numerical criterion specific to the DG method. In this work, e.g. as opposed to Duran and Marche (2015), the pre-balanced NSW equations were purposefully avoided to entirely keep the topography and its derivatives (up to third-order) as source terms. A hybrid topography discretization is adopted for treating these higher-order derivative terms using a local fourth-order DG expansion (DG4). The RKDG2-based model solving the GN equations is further supported with stable friction source term discretization and a conservative wetting and drying condition, to enable applicability for a range of tests involving nearshore wave processes with nonlinearity, dispersion, interaction with uneven and rough topographies and/or wetting and drying.

In what follows, Section 2 summarizes the GN model equations; Section 3 presents the details of the DG discretizations used including the details relevant to the integration of the topography source terms, treatment of wetting and drying and dispersive terms computations; Section 4 contains an exhaustive and systematic validation of the proposed model development over a series of selected test cases; Section 5 outlines the conclusions.

2- The Green-Naghdi (GN) equations

The standard one-dimensional (1D) GN system can be cast in an alternative form, which involves an optimization parameter and incorporates time-independent dispersive terms in diagonal matrices (Lannes and Marche 2015). This (so-called "one-parameter") model reads:

$$\begin{cases} \partial_t h + \partial_x (hu) = 0 \\ [1 + \alpha \mathbb{T}[h_b]] \left(\partial_t (hu) + \partial_x (hu^2) + \frac{\alpha - 1}{\alpha} gh\partial_x \zeta \right) + \frac{1}{\alpha} gh\partial_x \zeta + \\ h\big(Q_1(u) + gQ_2(\zeta)\big) + gQ_3 \left([1 + \alpha \mathbb{T}[h_b]]^{-1} (gh\partial_x \zeta) \right) = 0 \end{cases} \quad (1)$$

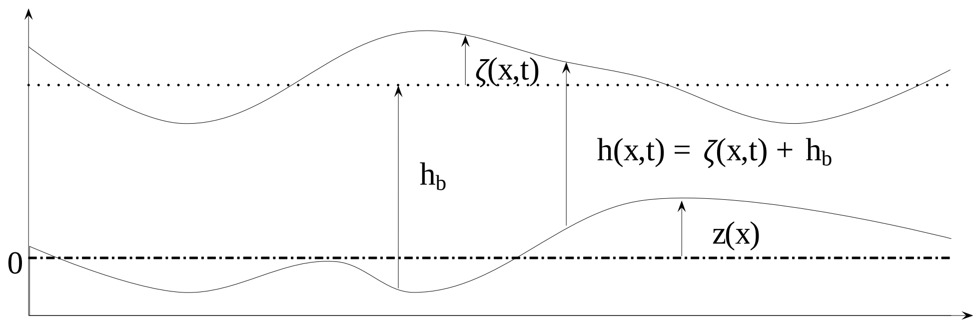

Fig. 1. Sketch of the free surface flow domain

where $u(x,t)$ is the horizontal velocity, h_b corresponds to the undisturbed state, $h(x,t) = \zeta(x,t) + h_b$ is the water height, $\zeta(x,t)$ stands for the free surface elevation and $z(x)$ is the variation of the bottom with respect to the rest state, as shown in Figure 1, and α is an optimization parameter. The differential operators $\mathcal{Q}_1$ and $\mathcal{Q}_2$ are expressed as follows:

$$\mathcal{Q}_1(u) = 2h\partial_x h(\partial_x u)^2 + \frac{4}{3}h^2\partial_x u(\partial_x^2 u) + h\partial_x z(\partial_x u)^2 + uh\partial_x u(\partial_x^2 z) + u^2\partial_x \zeta(\partial_x^2 z) + \frac{h}{2}u^2(\partial_x^3 z) \tag{2}$$

$$\mathcal{Q}_2(\zeta) = -\left(\partial_x\zeta\partial_x z + \frac{h}{2}\partial_x^2 z\right)\partial_x\zeta \tag{3}$$

For a given scalar function w, the second-order differential operator $\mathbb{T}$ is defined as:

$$\mathbb{T}[h_b](w) = -\frac{h_b^3}{3}\partial_x^2\left(\frac{w}{h_b}\right) - h_b^2\partial_x h_b\partial_x\left(\frac{w}{h_b}\right) \tag{4}$$

and $\mathcal{Q}_3$ admits the simplified notation:

$$\mathcal{Q}_3(w) = \frac{1}{6}\partial_x(h^2 - h_b^2)\partial_x w + \frac{h^2 - h_b^2}{3}\partial_x^2 w - \frac{1}{6}\partial_x^2(h^2 - h_b^2)w \tag{5}$$

Eq. (1) can be rewritten in the following form:

$$\begin{cases} \partial_t h + \partial_x(hu) = 0 \\ \partial_t(hu) + \partial_x(hu^2) + \dfrac{\alpha - 1}{\alpha}gh\partial_x\zeta + \left[1 + \alpha\mathbb{T}[h_b]\right]^{-1}\left[\dfrac{1}{\alpha}gh\partial_x\zeta + \right. \\ \left. h\big(\mathcal{Q}_1(u) + g\mathcal{Q}_2(\zeta)\big) + g\mathcal{Q}_3\left(\left[1 + \alpha\mathbb{T}[h_b]\right]^{-1}(gh\partial_x\zeta)\right)\right] = 0 \end{cases} \tag{6}$$

in which the differential operator $\left[1 + \alpha\mathbb{T}[h_b]\right]$ is factored out, making it possible not to compute third-order derivatives that are qualitatively present in Eq. (1). Replacing the free surface gradient term $gh\partial_x\zeta$ as:

$$gh\partial_x\zeta = \partial_x\left(\frac{1}{2}gh^2\right) + gh\partial_x z \tag{7}$$

Eq. (6) would become:

$$\begin{cases} \partial_t h + \partial_x(hu) = 0 \\ \partial_t(hu) + \partial_x(hu^2) + \partial_x\left(\dfrac{1}{2}gh^2\right) = -gh\partial_x z - \mathcal{D}_c \end{cases} \tag{8}$$

In which $\mathcal{D}_c$ accounts for the dispersive source term as:

$$\mathcal{D}_c = -\frac{1}{\alpha} gh\partial_x\zeta + \left[1 + \alpha\mathbb{T}[h_b]\right]^{-1}\left[\frac{1}{\alpha} gh\partial_x\zeta + h\big(\mathcal{Q}_1(u) + g\mathcal{Q}_2(\zeta)\big) + g\mathcal{Q}_3\left(\left[1 + \alpha\mathbb{T}[h_b]\right]^{-1}(gh\partial_x\zeta)\right)\right] \quad (9)$$

As explained in Lannes and Marche (2015), this GN formulation (i.e. the one-parameter model) is stabilized against high-frequency perturbations via the presence of the differential operator $\left[1 + \alpha\mathbb{T}[h_b]\right]^{-1}$, which can also be directly assembled in a preprocessing step. Based on these aspects, this alternative GN formulation is adopted here, which can be decomposed into a conservative form of the hyperbolic NSW equations plus elliptic source terms for adding on dispersive effects. Therefore, Eq. (8) could be presented in matrix conservative form as follows:

$$\partial_t\mathbf{U} + \partial_x\mathbf{F}(\mathbf{U}, z) = \mathbf{S}_\mathrm{b}(\mathbf{U}, z) + \mathbf{S}_\mathrm{f}(\mathbf{U}, z) - \mathbf{D}(\mathbf{U}, z) \quad (10)$$

$$\mathbf{U} = \begin{bmatrix} h \\ q \end{bmatrix}, \qquad \mathbf{F}(\mathbf{U}, z) = \begin{bmatrix} q \\ \frac{q^2}{h} + \frac{1}{2}gh^2 \end{bmatrix},$$

$$\mathbf{S}_\mathrm{b}(\mathbf{U}, z) = \begin{bmatrix} 0 \\ -gh\partial_x z \end{bmatrix}, \qquad \mathbf{S}_\mathrm{f}(\mathbf{U}, z) = \begin{bmatrix} 0 \\ -C_f u|u| \end{bmatrix}, \qquad \mathbf{D}(\mathbf{U}, z) = \begin{bmatrix} 0 \\ \mathcal{D}_c \end{bmatrix} \quad (11)$$

where **U** is the vector of flow variables, **F** represents the fluxes, $\mathbf{S}_\mathrm{b}$ shows the topography source terms and $\mathbf{S}_\mathrm{f}$ defines the friction source terms, in which $C_f = \frac{g n_M^2}{h^{1/3}}$ is the coefficient of bed roughness and n_M represents the Manning coefficient. The friction source terms, though were not included in the original formulation (Lannes and Marche, 2015), will be considered here as for the NSW equations.

To reduce the complexity of obtaining the dispersive source terms $\mathcal{D}_c$, Eq. (9) is reformulated in terms of the following coupled system:

$$\begin{cases} \left[I + \alpha\mathbb{T}[h_b]\right]\left(\mathcal{D}_c + \frac{1}{\alpha} gh\partial_x\zeta\right) = h\left(\frac{1}{\alpha} g\partial_x\zeta + \mathcal{Q}_1[h, z](u) + g\mathcal{Q}_2[h, z](\zeta)\right) + \mathcal{Q}_3[h, h_b]\mathcal{K} \\ \left[I + \alpha\mathbb{T}[h_b]\right]\mathcal{K} = gh\partial_x\zeta \end{cases} \quad (12)$$

in which $\mathcal{K}$ is an auxiliary variable and the respective terms are previously defined in Eqs. (2-5). As for the choice of optimization parameter α, Lannes and Marche (2015) recommended taking 1.159, which will also be adopted here.

3- RKDG2-based GN numerical solver

This section extends a robust RKDG2 numerical solver of the NSW with source terms considering wetting and drying (Kesserwani and Liang 2012). The RKDG2 method adopted here is particularly based on the conventional form of the NSW and supported with new technical measures to fit the case of the GN equations.

A 1D computational domain with a length of L, is divided by $N+1$ interface points $0 = x_{1/2} < x_{3/2} < \cdots < x_{N+1/2} = L$, into N uniform cells, each cell $I_i = \left[x_{i-1/2}, x_{i+1/2}\right]$ being centered at $x_i = 1/2\left(x_{i+1/2} + x_{i-1/2}\right)$ and having a length of $\Delta x = x_{i+1/2} - x_{i-1/2}$. In the framework of a local DG approximation, a kth order polynomial solution of the flow vector, denoted by $\mathbf{U}_{\mathrm{h}}(x,t) = [h_{\mathrm{h}}, q_{\mathrm{h}}]^T$, is sought that belongs to the space of polynomials in I_i of degrees at most k (giving $k+1$ order of accuracy in space). To get a FE local weak formulation, Eq. (10) is multiplied by a test function v, then integrated by parts over the control volume I_i to give:

$$\int_{I_i} \partial_t \mathbf{U}_{\mathrm{h}}(x,t) v(x) dx - \int_{I_i} \mathbf{F}\big(\mathbf{U}_{\mathrm{h}}(x,t)\big)\partial_x v(x) dx + \left[\tilde{\mathbf{F}}\left(\mathbf{U}_{\mathrm{h}}\left(x_{i+1/2},t\right)\right) v\left(x_{i+1/2}\right) - \tilde{\mathbf{F}}\left(\mathbf{U}_{\mathrm{h}}\left(x_{i-1/2},t\right)\right) v\left(x_{i-1/2}\right)\right] = \int_{I_i} \mathbf{S}_{\mathrm{b}}(\mathbf{U}_{\mathrm{h}}(x,t), z_{\mathrm{h}}) v(x) dx - \int_{I_i} \mathbf{D}_{\mathrm{h}}(\mathbf{U}_{\mathrm{h}}(x,t), z_{\mathrm{h}})\, v(x) dx \tag{13}$$

in which, $\mathbf{D}_{\mathrm{h}}$ and z_{h} are local approximations of $\mathbf{D}$ and z, which are also spanned by FE expansion coefficients, and $\tilde{\mathbf{F}}$ is a nonlinear numerical flux function based on an approximate Riemann solver featuring in the FV philosophy (Toro and Garcia-Navarro, 2007).

The local approximate solutions are expanded into polynomial basis functions $\{\phi_l^i\}_l$ that is compactly supported on cell I_i, as:

$$\mathbf{U}_{\mathrm{h}}(x,t)|_{I_i} = \sum_{l=0}^{k} \mathbf{U}_i^l(t)\phi_l^i(x) \tag{14}$$

$$\mathbf{D}_{\mathrm{h}}(x,t)|_{I_i} = \sum_{l=0}^{k} \mathbf{D}_i^l(t)\phi_l^i(x) \tag{15}$$

where $\mathbf{U}_i^l$ and $\mathbf{D}_i^l$ are time-dependent expansion coefficients. In order to achieve a decoupled version of the Galerkin formulation, Eq. (13), the local basis functions $\{\phi_l^i\}_l$ have been defined according to the Legendre polynomials

$$\phi_l^i(x) = \phi_l\left(\frac{x - x_i}{\Delta x/2}\right) \tag{16}$$

where $\phi_l(X)$ are the L^2-orthogonal Legendre polynomials on their reference domain $[-1, 1]$:

$$\phi_l(X) = \frac{1}{2^k k!}\frac{d^l}{dX^l}(X^2 - 1)^l \tag{17}$$

3.1 RKDG2 method for the convective parts

By selecting $k = 1$ a second-order DG (DG2) discretization can be obtained in which the local solution is linear:

$$\mathbf{U}_{\mathrm{h}}|_{I_i} = \mathbf{U}_i^0(t) + \mathbf{U}_i^1(t)\left(\frac{x - x_i}{\Delta x/2}\right) \tag{18}$$

where the coefficients $\mathbf{U}_i^0(t)$ and $\mathbf{U}_i^1(t)$ can be viewed as average and slope coefficients, respectively. From an available initial conditions, i.e. $\mathbf{U}_0(x) = \mathbf{U}(x, 0)$, the initial state of the coefficients can be simplified to:

$$\mathbf{U}_i^0(0) = \frac{1}{2}\left(\mathbf{U}_0\left(x_{i+1/2}\right) + \mathbf{U}_0\left(x_{i-1/2}\right)\right) \tag{19}$$

$$\mathbf{U}_i^1(0) = \frac{1}{2}\left(\mathbf{U}_0\left(x_{i+1/2}\right) - \mathbf{U}_0\left(x_{i-1/2}\right)\right) \tag{20}$$

For topography discretization of convective parts, again, linear basis functions (k = 1) are used, and hence a similar expansion for the variable $z(x)$ can be obtained by means of constant coefficients z_i^0 and z_i^1:

$$z_{\mathrm{h}}|_{I_i} = z_i^0 + z_i^1\left(\frac{x - x_i}{\Delta x/2}\right) \tag{21}$$

so that its derivative is used in the evaluation of the topography source term, namely:

$$\frac{d}{dx} z_{\mathrm{h}}(x)|_{I_i} = \frac{2 z_i^1}{\Delta x} \tag{22}$$

The coefficients z_i^0 and z_i^1 are obtainable from the given topography function $z(x)$, i.e.:

$$z_i^0 = \frac{1}{2}\left(z\left(x_{i+1/2}\right) + z\left(x_{i-1/2}\right)\right) \tag{23}$$

$$z_i^1 = \frac{1}{2}\left(z\left(x_{i+1/2}\right) - z\left(x_{i-1/2}\right)\right) \tag{24}$$

With this treatment for the topography, it is easy to verify that the continuity property holds in particular across interface points $x_{i+1/2}$ and $x_{i-1/2}$. For example at interface $x_{i+1/2}$ shared by elements I_i and I_{i+1}, (23) and (24) yield:

$$z_{\mathrm{h}}(x_{i+1/2}^-)\big|_{I_i} = z_i^0 + z_i^1 = z\left(x_{i+1/2}\right) = z_{i+1}^0 - z_{i+1}^1 = z_{\mathrm{h}}(x_{i+1/2}^+)\big|_{I_{i+1}} \tag{25}$$

Substituting the expanded variables into the weak formulation, a decoupled system of ODEs results for the evolution of each of the average and slope coefficients:

$$\partial_t \mathbf{U}_i^0 = \mathbf{L}_i^0\left(\mathbf{U}_{i-1}^{0,1}, \mathbf{U}_i^{0,1}, \mathbf{U}_{i+1}^{0,1}\right)$$
$$\partial_t \mathbf{U}_i^1 = \mathbf{L}_i^1\left(\mathbf{U}_{i-1}^{0,1}, \mathbf{U}_i^{0,1}, \mathbf{U}_{i+1}^{0,1}\right) \tag{26}$$

where $\mathbf{L}_i^{0,1}$ represent discrete spatial operators, which may be expressed as follows:

$$\mathbf{L}_i^0 = -\frac{1}{\Delta x}\left[\tilde{\mathbf{F}}_{i+1/2} - \tilde{\mathbf{F}}_{i-1/2} + \Delta x\, \mathbf{S}_\mathrm{b}(\mathbf{U}_i^0, z_i^1)\right] - D_i^0(t) \tag{27}$$

$$\begin{aligned}\mathbf{L}_i^1 = -\frac{3}{\Delta x}\Big\{&\left(\tilde{\mathbf{F}}_{i+1/2} - \tilde{\mathbf{F}}_{i-1/2}\right) - \mathbf{F}\left(\mathbf{U}_i^0 + \hat{\mathbf{U}}_i^1/\sqrt{3}\right) - \mathbf{F}\left(\mathbf{U}_i^0 - \hat{\mathbf{U}}_i^1/\sqrt{3}\right)\\ &-\frac{\Delta x\sqrt{3}}{6}\left[\mathbf{S}_\mathrm{b}\left(\mathbf{U}_i^0 + \hat{\mathbf{U}}_i^1/\sqrt{3}, z_i^1\right) - \mathbf{S}_\mathrm{b}\left(\mathbf{U}_i^0 - \hat{\mathbf{U}}_i^1/\sqrt{3}, z_i^1\right)\right]\Big\} - D_i^1(t)\end{aligned} \tag{28}$$

where the “hat” symbol refers to the slope-limited coefficients resulting from the local slope-limiting process (see Section 3.4). In addition, the special numerical treatments regarding dry cells detection, numerical fluxes and friction source terms could be summarized as follows:

- The flux evaluations across cells interfaces $\tilde{\mathbf{F}}_{i\pm1/2}$ are achieved based on a two-argument numreical flux function $\tilde{\mathbf{F}}$, associted with the HLL solver.
- A threshold of $tolh_{dry} = 10^{-3}$ is used for dry cells detection based on internal evaluations considering four inner cell points (i.e. two Gaussian points and two interface points).
- For discretization of the friction source terms, a compound approach is deployed in which they are first calculated implicitly using a splitting method and then are explicitly discretized in Eqs. (27) and (28). This approach is aimed to avoid instabilities due to possible unphysically-reversed flow at drying zones (Murillo et al., 2009; Kesserwani and Liang, 2012).
- Ad-hoc wetting and drying condition is proposed in coherence with the current choice for the model equations and topography discretization (details in Section 3.1.1).

Finally, the average and slope coefficients are marched in time using a two-stage RK time integration method with a time step restricted by the CFL condition (i.e. with a Courant number smaller than 0.333 in respect of the analysis in Cockburn and Shu (1991) as follows:

$$\left(\mathbf{U}_i^{0,1}\right)^{n+1/2} = \left(\mathbf{U}_i^{0,1}\right)^{n} + \Delta t\left(\mathbf{L}_i^{0,1}\right)^{n} \tag{29}$$

$$\left(\mathbf{U}_i^{0,1}\right)^{n+1} = \frac{1}{2}\left[\left(\mathbf{U}_i^{0,1}\right)^{n} + \left(\mathbf{U}_i^{0,1}\right)^{n+1/2} + \Delta t\left(\mathbf{L}_i^{0,1}\right)^{n+1/2}\right] \tag{30}$$

3.1.1 Ad-hoc wetting and drying condition

In this work, the depth-positivity preserving reconstructions in Liang and March (2009) will be applied and simplified at the interfaces, however under the following hypotheses:

- The standard NSW equations (10)-(11) will be considered instead of the so-called pre-balanced form.
- There is no intermediate involvement of the free-surface elevation for ensuring depth-positivity preserving reconstructions.
- Topography continuity, i.e. at the interfaces, based on Eqs. (23)-(24), is ensured.

By denoting $\mathbf{U}_{i\pm1/2}^{\pm} = \mathbf{U}_{\mathrm{h}}\left(x_{i\pm1/2}^{\pm}\right) = \left[h_{i\pm1/2}^{\pm}, q_{i\pm1/2}^{\pm}\right]^{\mathrm{T}}$, $z_{i\pm1/2} = z_{\mathrm{h}}\left(x_{i\pm1/2}^{\pm}\right)$ to be values at the interfaces $x_{i+1/2}$ and $x_{i-1/2}$, respectively, well-balanced and positivity preserving versions can be obtained and will be appended with the superscript “star”:

$$h_{i-1/2}^{\pm,*} = \max\left(0, h_{i-1/2}^{\pm}\right) \quad \text{and} \quad q_{i-1/2}^{\pm,*} = h_{i-1/2}^{\pm,*} u_{i-1/2}^{\pm} \tag{31}$$

$$h_{i+1/2}^{\pm,*} = \max\left(0, h_{i+1/2}^{\pm}\right) \quad \text{and} \quad q_{i+1/2}^{\pm,*} = h_{i+1/2}^{\pm,*} u_{i+1/2}^{\pm} \tag{32}$$

where $u_{i-1/2}^{+} = q_{i-1/2}^{+}/h_{i-1/2}^{+}$ and $u_{i+1/2}^{-} = q_{i+1/2}^{-}/h_{i+1/2}^{-}$ when $h_{\mathrm{h}}|_{I_i} > tolh_{dry}$. Further to (31) and (32), the following (numerical) conditions for interface topography evaluations are necessary to also ensure the well-balanced property for partially wet cases, i.e. when the flow (from one side) is blocked by a dry obstacle (from the other side):

$$z_{i-1/2}^{*} = z_{i-1/2}^{*} - \max\left(0, -h_{i-1/2}^{+}\right) \quad \text{and} \quad z_{i+1/2}^{*} = z_{i+1/2}^{*} - \max\left(0, -h_{i+1/2}^{-}\right) \tag{33}$$

It may be worth noting that Eqs. (31-33) only act on potentially changing interface evaluations for the states of the flow and/or topography variables. These potential changes must then be used to consistently re-define "positivity-preserving coefficients", which can be done by reapplying Eqs. (19), (20), (23) and (24) to re-initialize the coefficients as a subsequent step to Eqs. (31-33). This will lead to revised coefficients for use in the DG2 operators (27-28), which will be appended by a "bar" symbol:

$$\bar{\mathbf{U}}_i^0(t) = \frac{1}{2}\left(\mathbf{U}_{i+1/2}^{-,*} + \mathbf{U}_{i-1/2}^{+,*}\right) \tag{34}$$

$$\bar{\mathbf{U}}_i^1(t) = \frac{1}{2}\left(\mathbf{U}_{i+1/2}^{-,*} - \mathbf{U}_{i-1/2}^{+,*}\right) \tag{35}$$

$$\bar{z}_i^0 = \frac{1}{2}\left(z_{i+1/2}^{*} + z_{i-1/2}^{*}\right) \tag{36}$$

$$\bar{z}_i^1 = \frac{1}{2}\left(z_{i+1/2}^{*} - z_{i-1/2}^{*}\right) \tag{37}$$

3.2 Dispersive terms computation

To consistently discretize the dispersive terms in Eq. (12), which have higher order derivatives, an alternative DG discretization approach (Cockburn and Shu, 1998) is used. In contrary to the work in Duran and Marche (2015), the mass and stiffness matrices obtained are diagonal, due to the adoption of the Legendre polynomials, hence resulting in a simpler structure. First, the following second-order Partial Differentiable Equation (PDE) for an arbitrary scalar valued function u is considered:

$$l - \partial_x^2 u = 0 \tag{38}$$

Defining an auxiliary variable w, the above equation could be rearranged as a set of two coupled first-order PDEs:

$$
\begin{aligned}
w + \partial_x u &= 0 \\
l + \partial_x w &= 0
\end{aligned}
\tag{39}
$$

Then, a weak formulation is obtained by multiplying the equations by a test function v, then integrating by parts over the control volume I_i:

$$
\begin{aligned}
&\int_{I_i} wv dx - \int_{I_i} u\, \partial_x v dx + \tilde{u}_{i+1/2} v\left(x_{i+1/2}\right) - \tilde{u}_{i-1/2} v\left(x_{i-1/2}\right) = 0 \\
&\int_{I_i} lv dx - \int_{I_i} w\, \partial_x v dx + \widetilde{w}_{i+1/2} v\left(x_{i+1/2}\right) - \widetilde{w}_{i-1/2} v\left(x_{i-1/2}\right) = 0
\end{aligned}
\tag{40}
$$

The interface fluxes $\tilde{u}$ and $\widetilde{w}$ are computed as (Cockburn and Shu, 1998):

$$
\begin{aligned}
\tilde{u} &= \bar{u} - \xi \langle u \rangle \\
\widetilde{w} &= \overline{w} + \sigma \langle w \rangle + \frac{\lambda}{\Delta x} \langle u \rangle
\end{aligned}
\tag{41}
$$

in which the interface average $\bar{u} = (u^+ + u^-)/2$ and jump $\langle u \rangle = (u^+ - u^-)/2$ are defined based on the right and left interface values u^+ and u^-, respectively. The value of upwind parameters, ξ and σ, and penalization parameter λ depends on the selected method to compute fluxes. Different approaches are available for computing these fluxes, e.g. the centered Bassi and Rebay (BR) approach and its stabilized version (sBR), the alternate upwind approach also known as Local Discontinuous Galerkin (LDG) and the Interior Penalty (IP) approach. In the present study the BR flux was avoided given its sub-optimal convergence rates (Duran and Marche, 2015). Among the other options, which can deliver optimal convergence rates (Kirby and Karniadakis, 2005; Eskilsson and Sherwin, 2006;

Steinmoeller et al., 2012, 2016), the LDG flux is chosen in this work and can be obtained by setting $\xi = \sigma = 1$ and $\lambda \neq 0$ (Cockburn and Shu, 1998).

In the same manner as the RKDG method, all variables in Eqs. (39) have local expansions. Setting the test functions equal to basis function ϕ and replacing the approximate solutions of variables, the global formulations of Eqs. (39) are obtained in matrix form as follows:

$$\begin{aligned} \mathbb{M}\mathbf{W} &= \mathbb{S}\mathbf{U} - (\mathbb{E} - \xi\mathbb{F})\mathbf{U} \\ \mathbb{M}\mathbf{L} &= \mathbb{S}\mathbf{W} - (\mathbb{E} + \nu\mathbb{F})\mathbf{W} - \frac{\lambda}{h}\mathbb{F}\mathbf{U} \end{aligned} \tag{42}$$

where $\mathbf{W}$, $\mathbf{U}$, and $\mathbf{L}$ are vectors of expansion coefficients of w, u and l, respectively. $\mathbb{M}$ and $\mathbb{S}$ are the mass and stiffness matrices which have a block diagonal structure:

$$\mathbb{M} = \begin{bmatrix} \mathbf{M}_1 & & \\ & \ddots & \\ & & \mathbf{M}_N \end{bmatrix}, \qquad \mathbb{S} = \begin{bmatrix} \mathbf{S}_1 & & \\ & \ddots & \\ & & \mathbf{S}_N \end{bmatrix} \tag{43}$$

where each block is of the form:

$$M_{jk}^i = \int_{I_i} \phi_j^i \phi_k^i dx, \qquad S_{jk}^i = \int_{I_i} \phi_j^i \frac{d}{dx} \phi_k^i dx \tag{44}$$

Because of adopting the Legendre polynomials as basis functions, the mass and stiffness matrices are diagonal, resulting in a simpler structure especially when the order of the method increases. Matrices $\mathbb{E}$ and $\mathbb{F}$ which account for the interface fluxes, have the following block tri-diagonal structure:

$$
\mathbf{E} = \begin{pmatrix}
-1/2 & 3/2 & 1/2 & -1/2 & & & & & & \\
3/2 & -1/2 & 1/2 & -1/2 & & & & & & \\
-1/2 & -1/2 & 0 & 1 & 1/2 & -1/2 & & & & \\
1/2 & 1/2 & 1 & 0 & 1/2 & -1/2 & & & & \\
 & & \ddots & & \ddots & & & \ddots & & \\
 & & & \ddots & & \ddots & & & \ddots & \\
 & & & & -1/2 & -1/2 & 0 & 1 & 1/2 & -1/2 \\
 & & & & 1/2 & 1/2 & 1 & 0 & 1/2 & -1/2 \\
 & & & & & & -1/2 & -1/2 & 1/2 & 3/2 \\
 & & & & & & 1/2 & 1/2 & 3/2 & 1/2
\end{pmatrix} \tag{45}
$$

$$
\mathbf{F} = \begin{pmatrix}
-1/2 & -1/2 & 1/2 & -1/2 & & & & & & \\
-1/2 & -1/2 & 1/2 & -1/2 & & & & & & \\
1/2 & 1/2 & -1 & 0 & 1/2 & -1/2 & & & & \\
-1/2 & -1/2 & 0 & -1 & 1/2 & -1/2 & & & & \\
 & & \ddots & & \ddots & & & \ddots & & \\
 & & & \ddots & & \ddots & & & \ddots & \\
 & & & & 1/2 & 1/2 & -1 & 0 & 1/2 & -1/2 \\
 & & & & -1/2 & -1/2 & 0 & -1 & 1/2 & -1/2 \\
 & & & & & & 1/2 & 1/2 & -1/2 & 1/2 \\
 & & & & & & -1/2 & -1/2 & 1/2 & -1/2
\end{pmatrix} \tag{46}
$$

Finally, the first and second order derivative operators are obtained as:

$$\mathbf{W} = -\mathbb{D}_x \mathbf{U}, \quad \mathbf{L} = \mathbb{D}_x^2 \mathbf{W} \tag{47}$$

where:

$$\mathbb{D}_x = -\mathbb{M}^{-1}(\mathbb{S} - \mathbb{E} + \xi \mathbb{F}) \tag{48}$$

$$\mathbb{D}_x^2 = \mathbb{M}^{-1}\left(-(\mathbb{S} - \mathbb{E} - \nu \mathbb{F})\mathbb{D}_x - \frac{\lambda}{h}\mathbb{F}\right) \tag{49}$$

Deploying these differentiation matrices, all the derivatives and nonlinear products could be computed. For solving the differential matrices there are several choices, e.g. Duran and Marche (2015) used the LU Factorization method. Here, the block tri-diagonal matrices were solved by block forward and back substitution and since they were diagonally dominant, no pivoting was required.

3.3 Fourth-order bed projection for the dispersive terms

Another consideration regarding the discretization of the dispersive terms is how to handle the associated local bed projection. In contrast to the convective part where the bed projection is linear, the dispersive source terms entail third-order derivatives for the topography, which hence means that a fourth-order Discontinuous Galerkin (DG4) approximation is needed ($k = 3$) to accountably achieve this operation. Such a local expansion for the topography has the following form:

$$z_{\mathrm{h}}(x)|_{I_i} = \sum_{l=0}^{k} z_i^l \phi_l^i(x) = z_i^0 \phi_0(X) + z_i^1 \phi_1(X) + z_i^2 \phi_2(X) + z_i^3 \phi_3(X) \tag{50}$$

in which $X = \frac{x - x_i}{\Delta x/2}$, and $\phi_l(X)$ are the L^2-orthogonal Legendre polynomials, as previously introduced in Eq. (17). These polynomials are written as:

$$\phi_0(X) = 1, \quad \phi_1(X) = X, \quad \phi_2(X) = \frac{1}{2}(3X^2 - 1), \quad \phi_3(X) = \frac{1}{2}(5X^3 - 3X) \tag{51}$$

The derivatives of the topography can be obtained by differentiating Eq. (50) with respect to x, i.e.

$$\partial_x\left[z_{\mathrm{h}}(x)|_{I_i}\right] = z_i^0 \partial_x[\phi_0(X)] + z_i^1 \partial_x[\phi_1(X)] + z_i^2 \partial_x[\phi_2(X)] + z_i^3 \partial_x[\phi_3(X)] \tag{52}$$

Inserting the derivatives of polynomials into Eq. (52) results in,

$$\partial_x\left[z_{\mathrm{h}}(x)|_{I_i}\right] = \frac{2}{\Delta x} z_i^1 + \frac{6X}{\Delta x} z_i^2 + \left(\frac{15X^2}{\Delta x} - \frac{3}{\Delta x}\right) z_i^3 \tag{53}$$

Recursive differentiating of Eq. (53) would result in higher derivatives as follows,

$$\partial_x^2\left[z_\mathrm{h}(x)|_{I_i}\right] = \frac{12}{\Delta x^2} z_i^2 + \frac{60X}{\Delta x^2} z_i^3 \tag{54}$$

$$\partial_x^3\left[z_\mathrm{h}(x)|_{I_i}\right] = \frac{120}{\Delta x^3} z_i^3 \tag{55}$$

In center of the cells, X equals to zero, therefore,

$$\partial_x\left[z_\mathrm{h}|_{I_i}\right] = \frac{2}{\Delta x} z_i^1 - \frac{3}{\Delta x} z_i^3 \tag{56}$$

$$\partial_x^2\left[z_\mathrm{h}|_{I_i}\right] = \frac{12}{\Delta x^2} z_i^2 \tag{57}$$

$$\partial_x^3\left[z_\mathrm{h}|_{I_i}\right] = \frac{120}{\Delta x^3} z_i^3 \tag{58}$$

The degrees of freedom for the topography $(z_i^3)_{l=0,1,2,3}$ are calculated as the projection of $z_\mathrm{h}(x)$ onto the space of approximating polynomials:

$$z_i^l = \frac{2l+1}{\Delta x}\int_{I_i} z_\mathrm{h}(x)\,\phi_l\left(\frac{x-x_i}{\Delta x/2}\right)dx \tag{59}$$

The integral terms are evaluated by Gaussian quadrature rule and result in the followings:

$$z_i^0 = \frac{1}{2}\left[z\left(x_{i+1/2}\right) + z\left(x_{i-1/2}\right)\right] \tag{60}$$

$$z_i^1 = \frac{\sqrt{3}}{2}\left[z\left(x_i + \Delta x\frac{\sqrt{3}}{6}\right) - z\left(x_i - \Delta x\frac{\sqrt{3}}{6}\right)\right] \tag{61}$$

$$z_i^2 = \frac{5}{9}\left[z\left(x_i + \Delta x\frac{\sqrt{15}}{10}\right) - 2z(x_i) + z\left(x_i - \Delta x\frac{\sqrt{15}}{10}\right)\right] \tag{62}$$

$$\begin{aligned} z_i^3 = 7\{&\mu\delta(20\delta^2 - 3)[z(x_i + \Delta x\delta) - z(x_i - \Delta x\delta)] \\ &+ \mu'\delta'(20\delta'^2 - 3)[z(x_i + \Delta x\delta') - z(x_i - \Delta x\delta')]\} \end{aligned} \tag{63}$$

where $\delta = 1/2\sqrt{(15 + 2\sqrt{30})/35}$, $\delta' = 1/2\sqrt{(15 - 2\sqrt{30})/35}$, $\mu = 1/4 - \sqrt{30}/72$ and $\mu' = 1/4 + \sqrt{30}/72$. It should be noted that quadrature weights and coefficients in Eqs. (60-63) are specific to a forth order approximation. In practice, topographic data are often provided as a set of discrete values and are generally difficult to be defined as a mathematical expression. Therefore, proper interpolation techniques are required which is not a straightforward issue (Kesserwani and Liang, 2011). In the present study, a simplified and practical consideration is used for determining z_i^l without involving direct calculation of the topographic values at the local points. Within a computational cell $I_i = [x_{i-1/2}; x_{i+1/2}]$, assuming that the discrete topographic data are available at its lower and upper limits, i.e. $z(x_{i-1/2})$ and $z(x_{i+1/2})$, the topography is defined linearly by $z(x_{i-1/2})$ and $z(x_{i+1/2})$ in cell I_i and the intermediate topographic data at $z\left(x_i \pm \Delta x \frac{\sqrt{3}}{6}\right)$ and $z\left(x_i \pm \Delta x \frac{\sqrt{15}}{10}\right)$ may then be obtained by linear interpolation. As a result the topography-associated degrees of freedom are written as:

$$z_i^0 = \frac{1}{2}\left[z(x_{i+1/2}) + z(x_{i-1/2})\right] \tag{64}$$

$$z_i^1 = \frac{1}{2}\left[z(x_{i+1/2}) - z(x_{i-1/2})\right] \tag{65}$$

$$z_i^2 = \frac{\sqrt{15}}{9}\left[z(x_{i+1/2}) - 2z_i^0 + z(x_{i-1/2})\right] \tag{66}$$

$$\begin{aligned} z_i^3 = 7\{&\mu\delta(20\delta^2 - 3)\left[2\delta z(x_{i+1/2}) - 2\delta z(x_{i-1/2})\right] \\ &+ \mu'\delta'(20\delta'^2 - 3)\left[2\delta' z(x_{i+1/2}) - 2\delta' z(x_{i-1/2})\right]\} \end{aligned} \tag{67}$$

3.4 Localized handling of wave breaking

To account for wave breaking, an approach for switching from the GN equations to the NSW equations is implemented and locally activated (i.e. to switch off dispersive source terms) when the wave is about to break. In this work, wave breaking detection has been achieved by a numerical criterion (instead of deploying sophisticated physical parameters, as discussed in Section 1). This criterion is specific to the DG method's superconvergence behavior, which is also used for shock detection in order to restrict the operation of the slope limiter (Krivodonova et al., 2004). In summary, regions of potential instability where switching should occur are here identified according to the following sensor:

$$\mathbf{DS}_{i+1/2}^{-} > \mathbf{1.0} \quad \boldsymbol{or} \quad \mathbf{DS}_{i-1/2}^{+} > \mathbf{1.0} \tag{68}$$

where $\mathbf{DS}_{i+1/2}^{-}$ and $\mathbf{DS}_{i-1/2}^{+}$ are the discontinuity detectors at the two cell edges ($x_{i+1/2}$ and $x_{i-1/2}$) within cell I_i (Kesserwani and Liang, 2012). The expression for $\mathbf{DS}_{i+1/2}^{-}$ is given by

$$\mathbf{DS}_{i+1/2}^{-} = \frac{\left|\mathbf{U}_{i+1/2}^{+} - \mathbf{U}_{i+1/2}^{-}\right|}{\left|\frac{\Delta x}{2}\right| \max\left(\left|\mathbf{U}_i^0 - \mathbf{U}_i^1/\sqrt{3}\right|, \left|\mathbf{U}_i^0 + \mathbf{U}_i^1/\sqrt{3}\right|\right)} \tag{69}$$

and $\mathbf{DS}_{i-1/2}^{+}$ is defined by analogy. It is worth nothing that once (68) switches the RKDG2 model to solving the NSW equations, it has been found necessary not to let the model return to the GN equations or otherwise the model may experience instabilities in the vicinity of the breaking point. It is also useful to stress out that another version of the sensor in Eq. (68) has been used for the detection of local cells that are in need for slope limiting, based however on a higher threshold value of 10.

4- Model verification and validation

This part will demonstrate the performance of the proposed RKDG2-GN model in predicting wave propagation and transformation through comparisons with analytical and experimental data. The inlet and outlet boundary conditions will depend on the test as detailed in the following. For quantitative analysis, errors and orders of accuracy are calculated based on the L^2-norms per number of cells N, i.e. as follows:

$$Error = \frac{1}{N} \frac{\|U_{exact} - U_{numerical}\|_2}{\|U_{exact}\|_2} \tag{70}$$

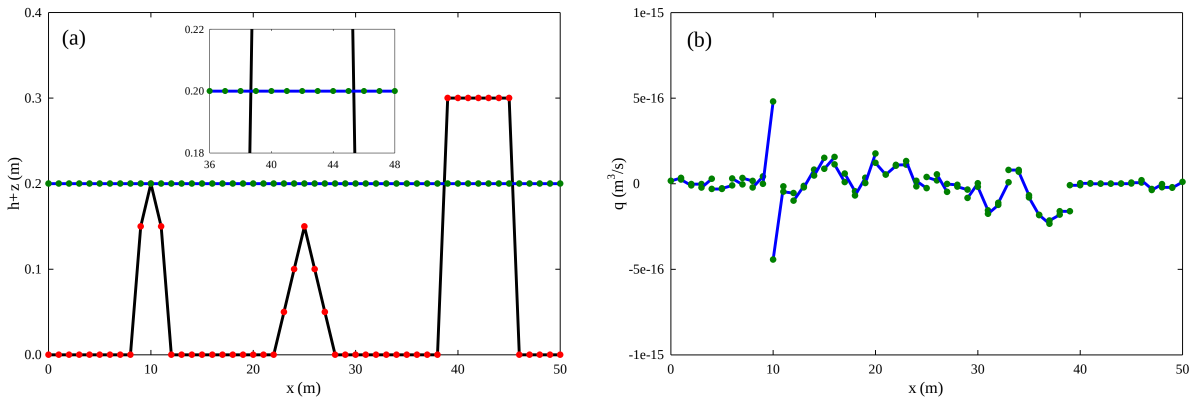

Fig. 2. Motionless flow over different patterns for the topography and wetting and drying. Computed full RKDG2 solution (blue lines) of: (a) free surface elevation, (b) the flow rate. Also included the interface points of the RKDG2 solutions (green dots), the continuous DG2 projection of the topography (black lines) and its interface evaluations (red dots)

4.1 Quiescent flow over an irregular bed

This test has been aimed and designed to validate the well-balanced, or conservative property of the proposed model over a domain that simultaneously involves various topography shapes ranging from smooth hump-like to sharp building-like geometries, and also considering wet and dry zones. The topography shapes are defined in Eq. (71) below.

$$z(x) = \begin{cases} 0.2 - 0.05(x-10)^2 & 8 < x \le 12 \\ 0.05x - 1.1 & 22 < x \le 25 \\ -0.05x + 1.4 & 25 < x \le 28 \\ 0.3 & 39 < x \le 46 \\ 0 & elsewhere \end{cases} \tag{71}$$

The still initial conditions are given by:

$$hu = 0, \quad h + z = 0.2 \tag{72}$$

Eq. (71) enables to distinguish three important scenarios for assessing the conservation property with wetting and/or drying, i.e. at a drying point at x = 10 m, for a wet case over a sharp topography gradient at x = 25 m and when the wet-dry front results from an intersection with a dry building at x = 39 and 46 m (see Figure 2a). The computational domain, of length 50 m, is divided into 50 cells and the model is run up to 100 seconds. Figure 2 reveals the behavior of the full RKDG2-GN (linear) solutions, showing clearly still steady state of the free surface elevation (i.e. Figure 2a) and slightly perturbed local solutions for the flow rate (i.e. Figure 2b) that, although illustrative of the discontinuous character, remain within machine precision error (1×10^{-16}). These results hence indicate that the proposed numerical model verify the well-balanced property, which should hold irrespective of the mesh size. In particular, looking at the zoom in portion in Figure 2a, the proposed scheme remains stable for the well-balanced property when the local linear solution cut through the dry step-like obstacle, which is likely to yield practical conveniences (e.g. negating the need for expanding significant amount of time for treating the presence of building within the mesh). Notable also, the magnitude of dispersive terms has been observed to be in the range of machine precision, indicating that the proposed RKDG2-GN model will not predict any spurious flows when handling potentially realistic flow scenarios involving highly irregular topography shapes and wetting and/or drying.

4.2 Oscillatory flow in a parabolic bowl

This test is mainly featured by moving wet-dry interfaces over an uneven topography and is known to be challenging for NSW-based numerical models. It is here considered to assess many properties of the proposed GN model. It consists of an oscillatory flow taking place inside a convex parabolic topography. The bed topography is described by $z(x) = h_0(x/a)^2$ with constants h_0 and a. By assuming a friction source term proportional to the velocity, i.e. $S_f = -\tau\, hu$ (τ is a constant friction factor), the analytical solution would be (Sampson, 2009):

$$\eta(x,t) = h_0 + \frac{a^2 B^2 e^{-\tau t}}{8g^2 h_0}\left(-s\tau \sin 2st + \left(\frac{\tau^2}{4} - s^2\right)\cos 2st\right) - \frac{B^2 e^{-\tau t}}{4g} - \frac{e^{-\tau t/2}}{g}\left(Bs\cos st + \frac{\tau B}{2}\sin st\right)x \qquad (73)$$

$$u(x,t) = Be^{-\tau t/2}\sin st$$

where B is a constant and $s = \sqrt{8gh_0 - \tau^2 a^2}/2a$. The computational domain is considered to have a length L = 14,000 m, i.e. [-7000 m; 7000 m], and the problem constants are selected to be: $h_0 = 11$ m, $a = 4000$ m and $B = 9$ m/s. According to the value of τ, a frictionless and a frictional sub-case can be considered. When $\tau = 0$, the frictionless sub-case is obtained in which the flow is expected to oscillate indefinitely with a period of $T = 1711$ s; whereas when $\tau > 0$, here equal to $0.0015\ \mathrm{s}^{-1}$, friction effects will be activated inducing a frictional flow that will be expected to decay with time until reaching a steady state.

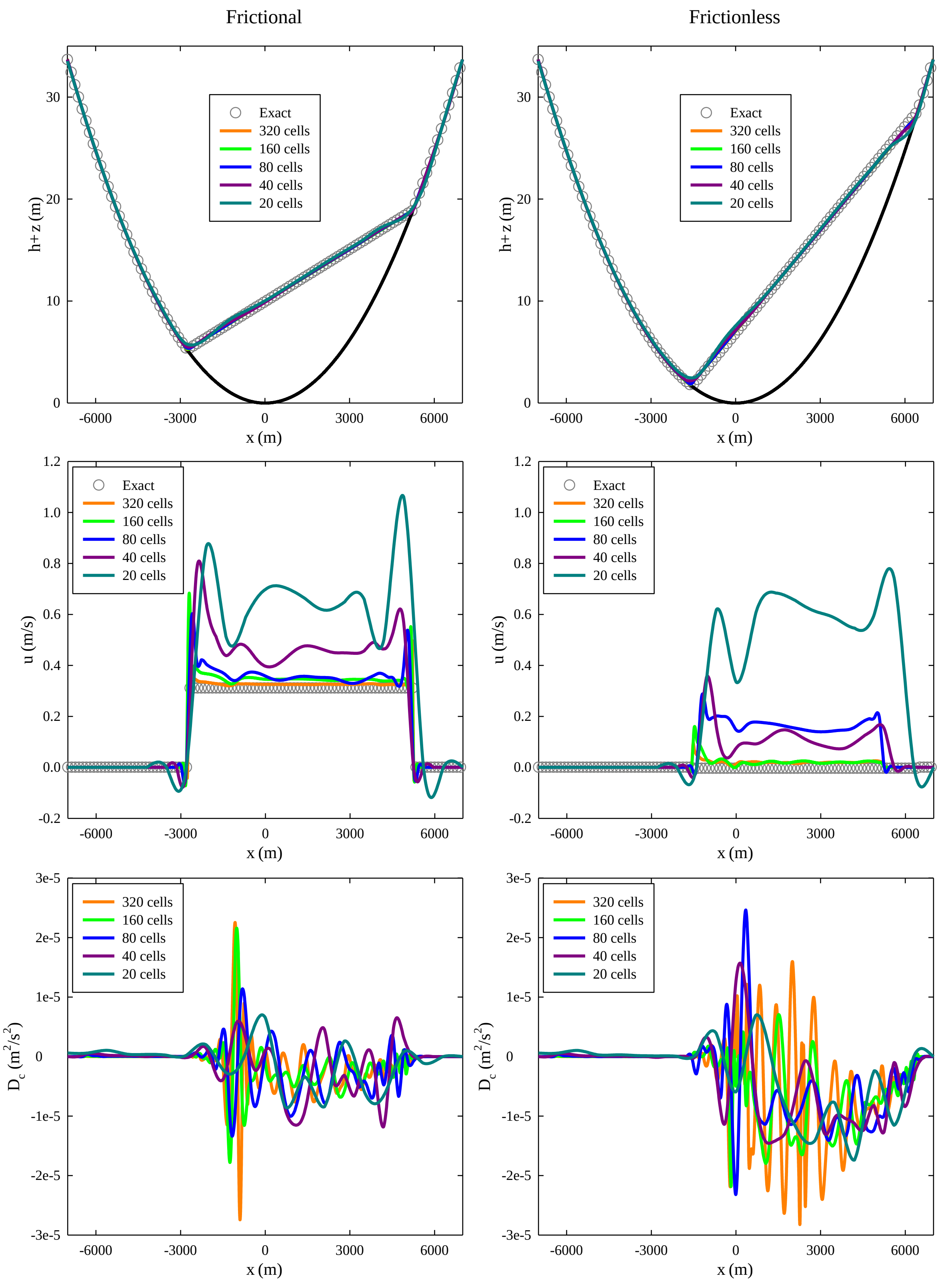

Fig. 3. Oscillatory flow in a parabolic bowl, numerical vs. analytical solutions at t = T / 2. From top: free surface elevation, velocity and magnitude of dispersive terms

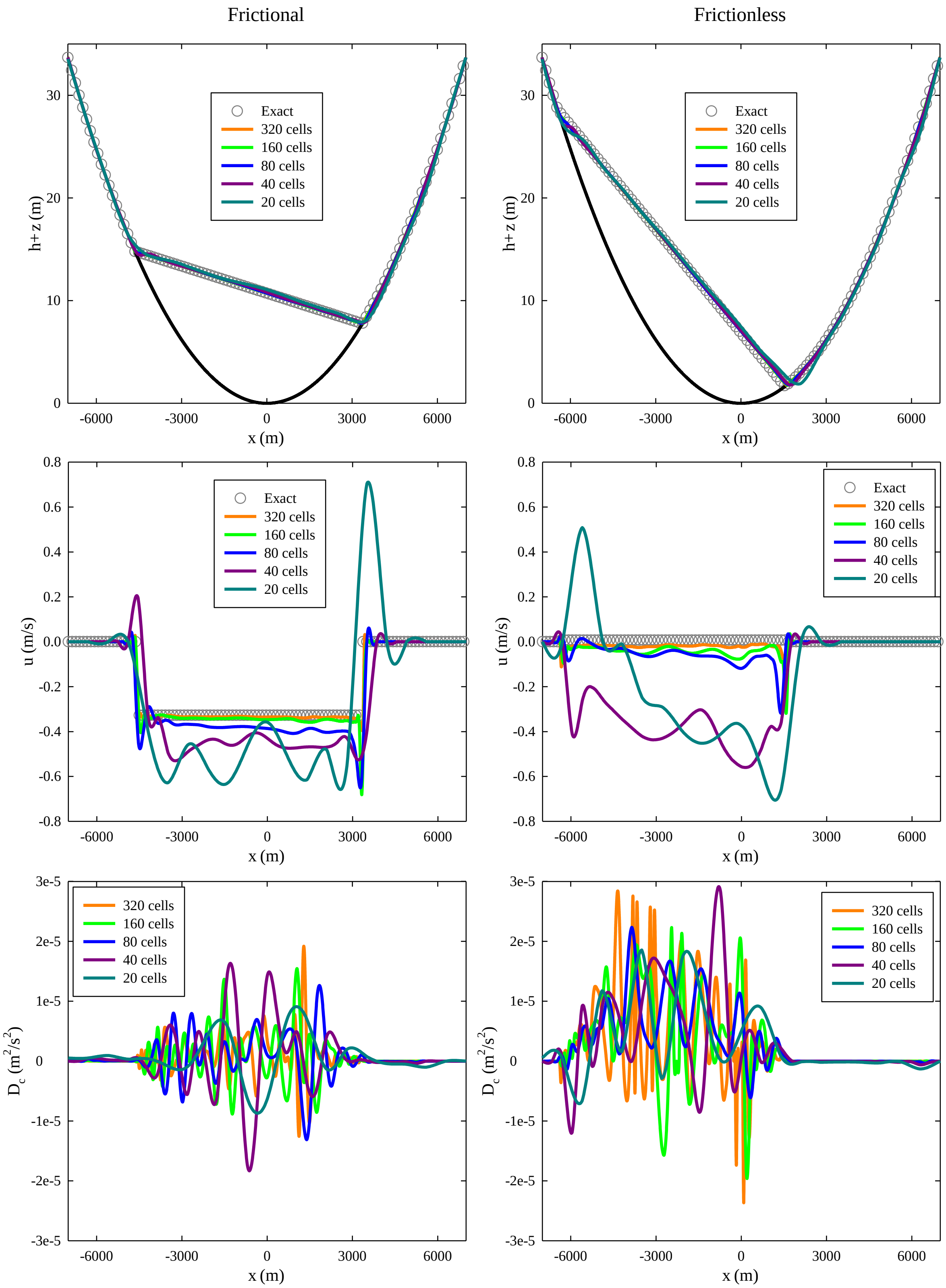

Fig. 4. Oscillatory flow in a parabolic bowl, numerical vs. analytical solutions at t = T. From top: free surface elevation, velocity and magnitude of dispersive terms

Figures 3 and 4 compare simulated results obtained on different meshes (i.e. involving 20, 40, 80, 160 and 320 computational cells) with the analytical solutions for both frictional and frictionless sub-cases at $t = T/2$ and $t = T$, respectively. In terms of predictability of the free surface elevation (Figures 3 and 4 – upper part), the simulations involving more than 40 cells are seen to agree very well with analytical solution. However the velocity predictions (Figures 3 and 4 – middle part) seems to be more illustrative about the impact of the mesh size on the simulations, clearly indicating that more cells would be needed (i.e. ≥ 80 cells for the frictional case and ≥ 160 cells for the frictionless case) in order to fairly capture the trail of the vanishing velocity due to the moving wet-dry front. As to the spikes occurring in the vicinity of the wet-dry fronts, they are commonly observed discrepancies for such a test and would be expected to slightly reduce with mesh refinement (e.g. Kesserwani and Wang, 2014). Figures 3 and 4 (lower part) include a view of the dispersive terms, which have a negligible magnitude, as expected for this kind of shallow flow, and a bounded variation (even after a longer time evolution, i.e. until t = 18T in our case). These results, supported also with the results in Section 4.1, indicate that the nonlinear and dispersive terms associated with extra source term, **D,** does not interfere with the stability of the proposed GN numerical solver when faced with dynamic wetting and drying processes over rough topographies.

To investigate the conservation property of the present model, the time evolution of the domain-integrated total energy was computed over 18T, which writes:

$$E(t) = \int_{-L/2}^{+L/2} \left(\frac{1}{2}hu^2 + \frac{1}{2}g\eta^2\right) dx \tag{74}$$

Following the work in Steinmoeller et al. (2012), this quantity is normalized by its initial value E_0 and then recorded over time for two of the meshes (i.e. with 80 and 160 cells) considering both frictional and frictionless cases. The normalized total energy histories are plotted in Figure 5 with the histories produced by the use of the exact solution (Eq. 73).

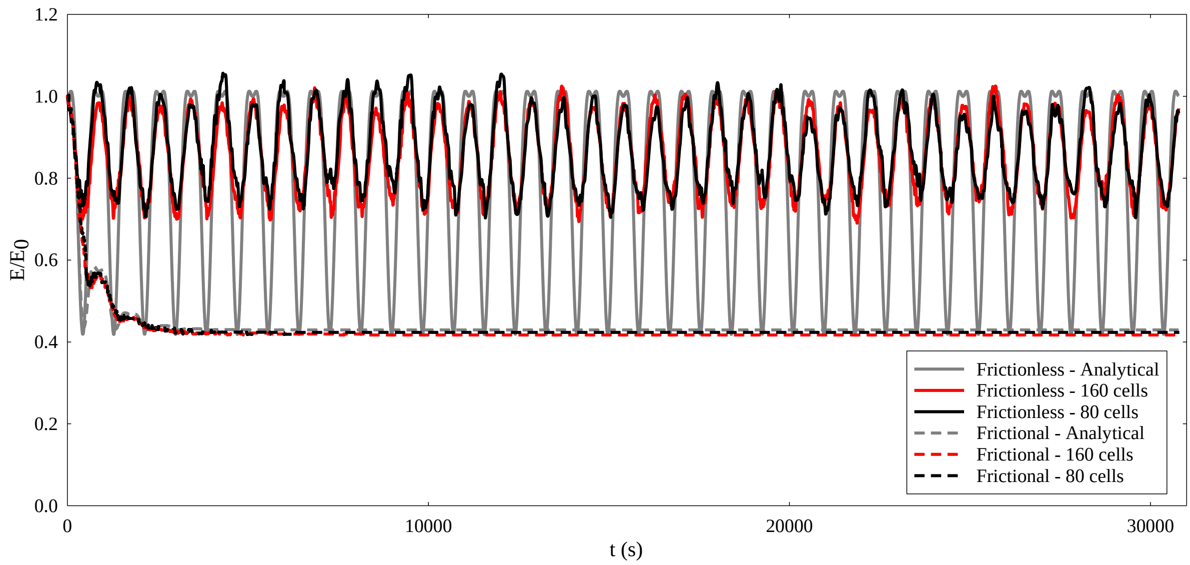

Fig. 5. Oscillatory flow in a parabolic bowl; domain-integrated total energy time histories after a long time simulation (i.e. t = 18T**).**

In both sub-cases, the normalized energy variation seems to be consistent despite the mesh size. For the frictional sub-case, the observed drop of energy level after some time is expected as the kinetic energy is proportional to the friction factor; however, after this drop, the remaining energy line remains constant, suggesting that there is no notable diffusivity in the proposed numerical scheme. As for the frictionless sub-case, the energy line appears to remain constant albeit with an oscillatory pattern, which is likely to be related to vanishing velocity as a result of the constant wetting and drying as can be noted from the exact profile. For the latter sub-case, the numerical model does not seem to be able to catch up with the analytical energy line at those instants where velocity vanishes after drying (i.e. when the kinetic energy instantaneously drops to zero). However, as can be seen in the frictional sub-case, such an impact from the vanishing velocity after drying reduces as the velocity magnitude drops. Despite this discrepancy, the evolution of the total energy line, in both cases, shows no signal of a drop throughout the simulation, reinforcing that the presented RKDG2-GN model is conservative.

Finally, an accuracy-order analysis (Table 1) is provided based on the errors generated from the results of the frictional sub-case at $t = T$. The numerical orders in the table show that the model is able to deliver second-order convergence rates, achieving on average orders of 2.2 and 2.3 for the depth and discharge variables, resp. These results further imply that the accuracy of the proposed RKDG2-GN model will be preserved even while coping with nearshore water simulations.

Table 1: Errors and orders of accuracy for parabolic bowl flow (frictional)

No. of elements	h		q	
	L^2-error	L^2-order	L^2-error	L^2-order
20	7.95E-04	--	3.23E-02	--
40	1.88E-04	2.08	9.97E-03	1.72
80	3.73E-05	2.33	2.25E-03	2.14
160	7.80E-06	2.25	3.41E-04	2.72
320	1.25E-06	2.64	6.93E-05	2.30

4.3 Propagation of a solitary wave

For accuracy assessment of dispersive wave behavior, a solitary wave propagating with a celerity c in the still water of depth h_0 is considered. The exact solution of the solitary wave that is similar in shape to solitons predicted by Korteweg-de Vries (KdV) equations (Steinmoeller et al., 2012), which is given by:

$$\begin{gathered} h(x,t) = h_0 + a\,\mathrm{sech}^2\left(\frac{\sqrt{3a}}{2h_0\sqrt{h_0+a}}(x-ct)\right) \\ u(x,t) = c\left(1 - \frac{h_0}{h(x,t)}\right) \end{gathered} \tag{75}$$

where $c = \sqrt{g(h_0 + a)}$ is the wave celerity. The first case demonstrates the propagation of a highly nonlinear solitary wave in a 200 m long channel with a reference water depth of $h_0 =$

1 m, and an amplitude of $a = 0.2$ m, initially centered at $x_0 = 50$ m. Figure 6 compares the predicted wave profiles at different instants with the exact solution, the results in Duran (2014) on a mesh with 400 cells and our results on meshes with 400, 300 and 200 cells.

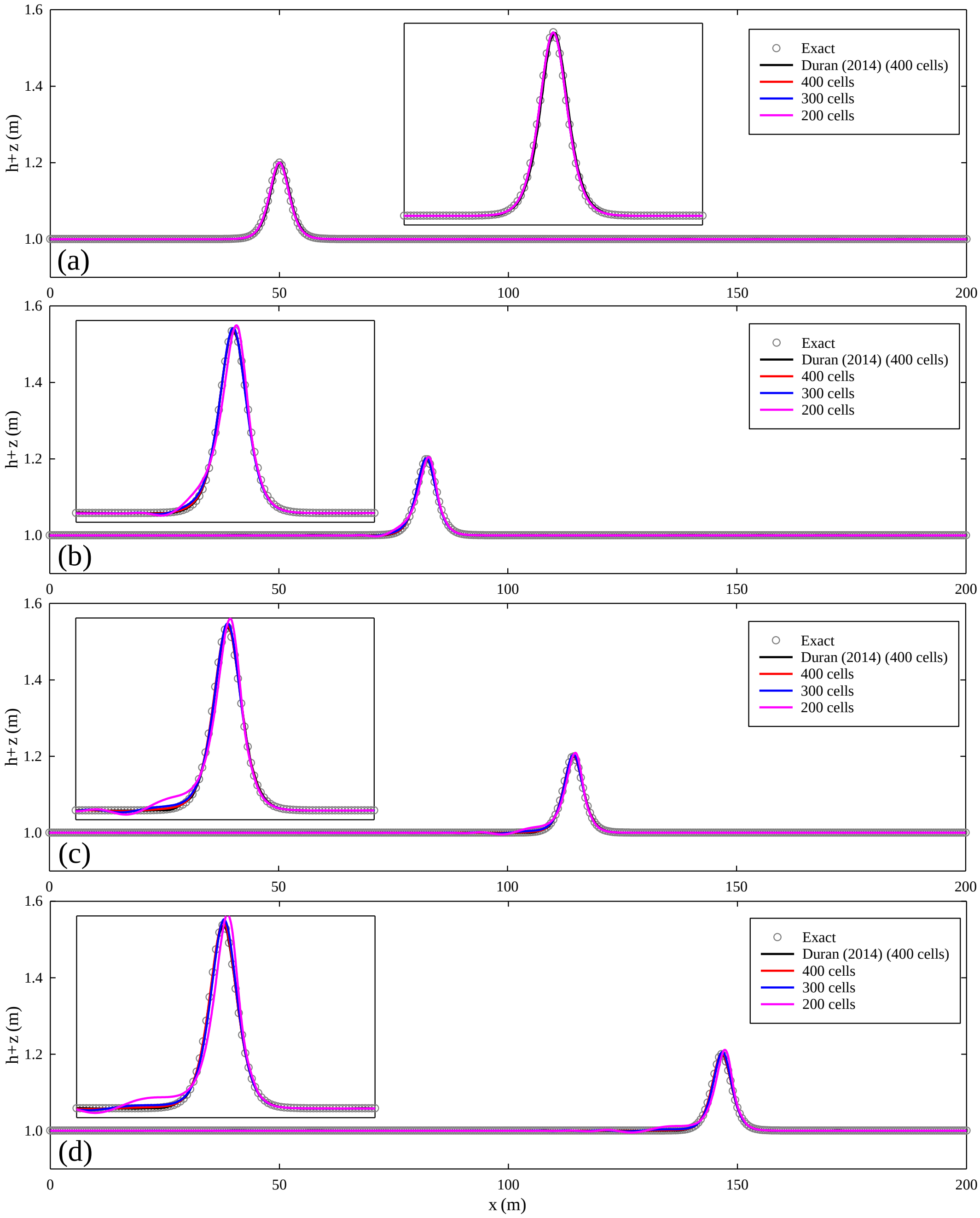

Fig. 6. Comparison of solitary wave profiles at (a) t = 0, (b) t = 9.4, (c) t = 18.75 (d) t = 28.15 seconds, for exact analytical solution, numerical results of Duran (2014) using 400 cells, and the present model using 400, 300 and 200 cells.

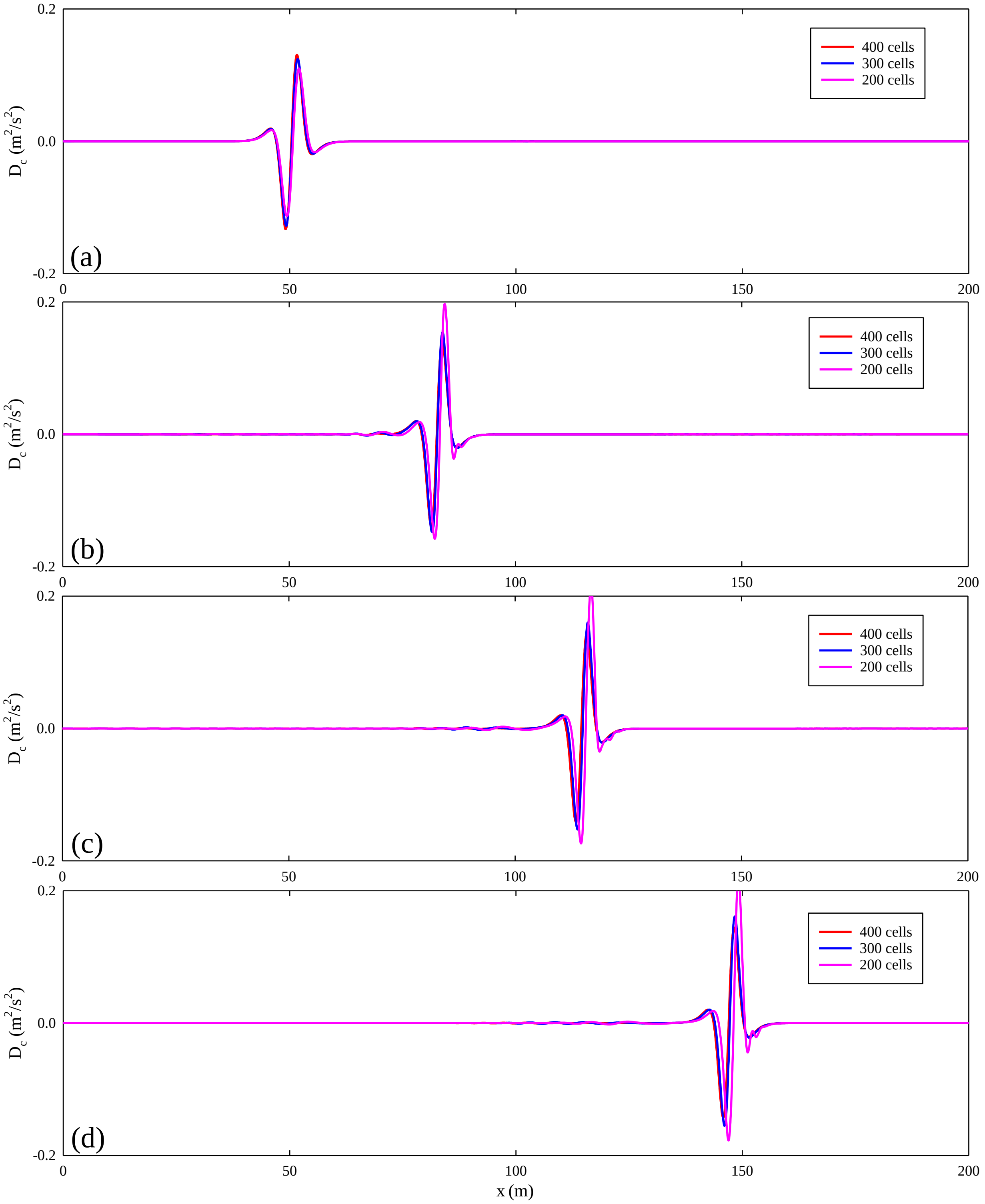

Fig. 7. Comparison of magnitudes of the dispersive source terms for the solitary wave at (a) t = 0, (b) t = 9.4, (c) t = 18.75 (d) t = 28.15 seconds

Zoom-in portions of the wave are also included for allowing close qualitative comparisons. On the finest mesh of 400 cells, the proposed RKDG2-GN predictions are seen to be comparable with the predictions made in Duran (2014) using an RKDG3-GN approach on the same mesh, both agreeing well with the exact solution at all the output times. On the medium mesh of 300 cells, the RKDG2-GN predictions preserve a good agreement with results on finer meshes and the exact solution, which implies that the proposed RKDG2-GN can deliver the level of fidelity required despite being less costly and complex.

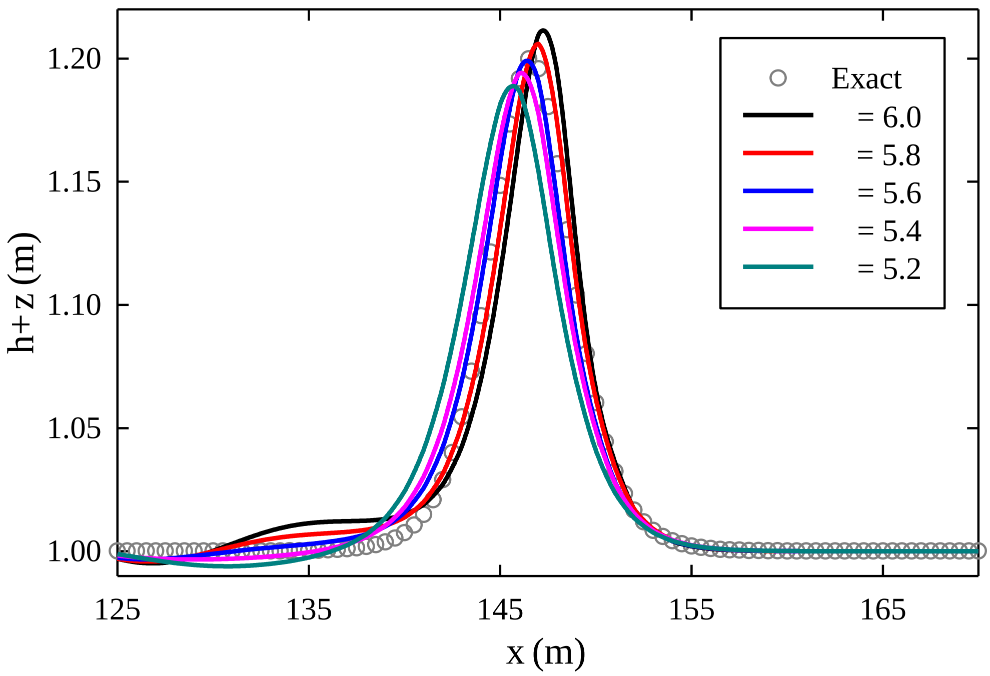

Fig. 8. Comparison of solitary wave profiles with 200 cells using respective penalization parameters (λ) at t = 28.15 s

As to the RKDG2-GN results on the coarsest mesh of 200 cells, our results can be said to be acceptable in terms of not being dissipative for the wave prediction, though it underperforms at the trailing wave (e.g. at t = 28.15 s). There, a larger amplitude is predicted when the coarse grid is used, which is not observed for the results on the finer meshes. Figure 7 further provides a view on the evolution of the dispersive terms, which shows inconsistently larger amplitude predictions on the coarsest mesh considered. However, these larger amplitudes seem to vanish by altering the penalization parameter of the LDG fluxes, e.g. when the λ parameter is equal to 5.6 as reveals Figure 8. This means that a user is likely to have the option to retain a fairly coarse mesh for this type of simulations, but may have to cope with more sensitive tuning for the parameters involved in the dispersive term solver.

Table 2: Errors and orders of accuracy for depth and discharge for solitary wave propagation

No. of elements	h		q	
	L^2-error	L^2-order	L^2-error	L^2-order
20	1.21E-03	--	8.83E-02	--
40	1.86E-04	2.70	6.60E-03	3.74
80	4.08E-05	2.19	1.54E-03	2.10
160	7.24E-06	2.50	2.63E-04	2.55
320	7.34E-07	3.30	2.69E-05	3.29
640	1.76E-07	2.05	6.80E-06	1.99

For a quantitative analysis, orders of accuracy (listed in Table 2) for free surface and discharge are computed based on errors associated with simulations on meshes with 20 to 640 cells. On average, an order of 2.54 and 2.73 for the depth and discharge were achieved by the proposed RKDG2-GN solver, which are in the range of the orders achieved by other GN models based on a second-order formulation (e.g. Panda et al., 2014; Li et al., 2014). It may be useful to report that the contribution of the dispersive effects, which was noted significant for this test (i.e. ranging between $|D_c| < 0.2$, see Figure 7), could be responsible for the slightly higher average (numerical) orders acquired here (as also observed in the investigation in Duran (2014)).

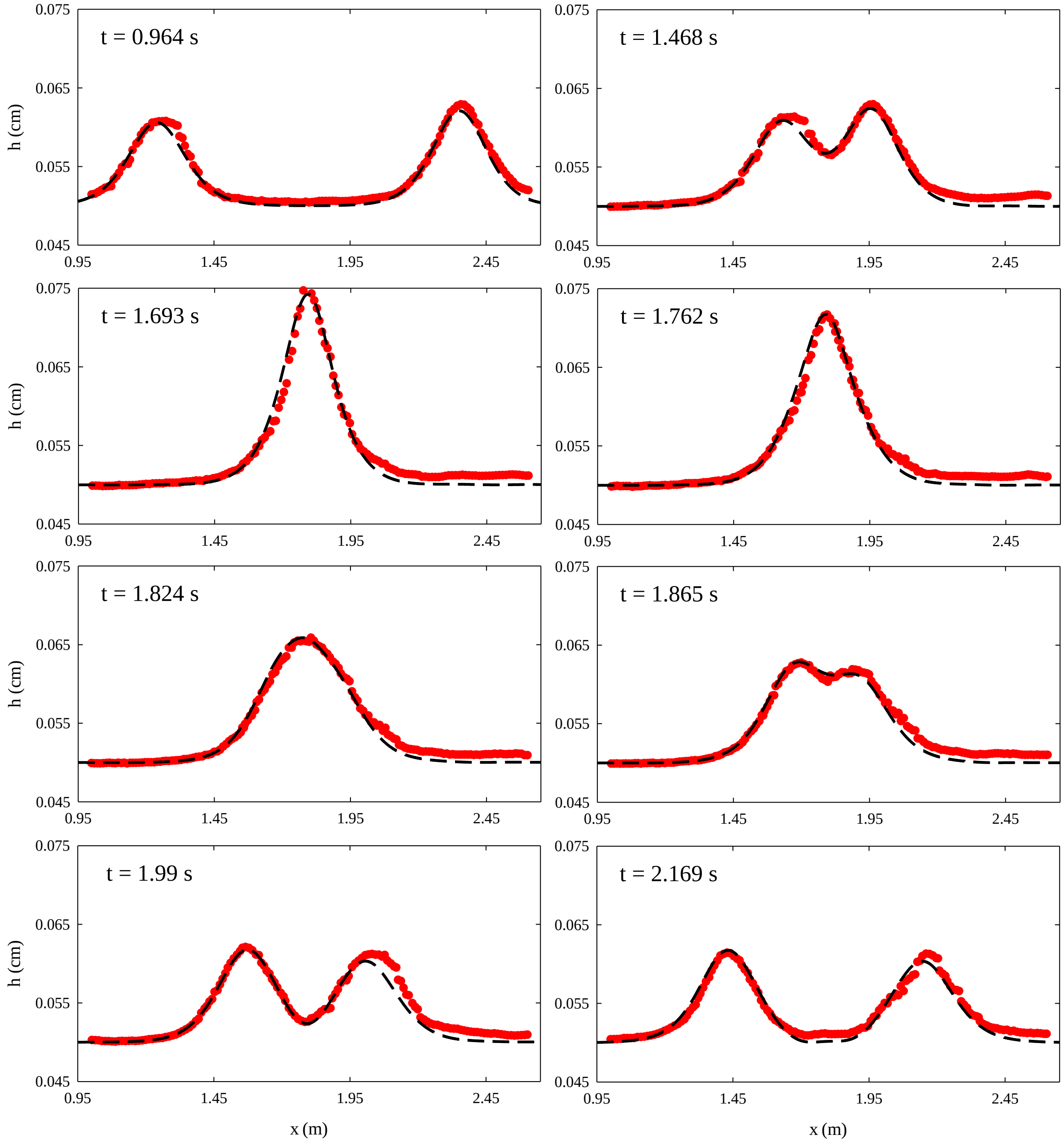

Fig. 9. Free surface profiles of head-on collision of two solitary waves, between numerical (dashed line) and experimental data of Craig et al. (2006) (dots).

In order to perform further analysis on nonlinear and dispersive effects, the head-on collision of two solitary waves propagating in opposite directions has also been investigated. The experimental data of this case is based on Craig et al. (2006), which consists of a 3.6 m long flume for with still water depth of $h_0 = 5$ cm. The two waves are initially located at x = 0.5 m and x = 3.1 m with the amplitudes equal to $a_1 = 1.063$ cm and $a_2 = 1.217$ cm, respectively. The simulations are conducted using N = 360 elements. Figure 9 shows the free surface profiles at different times, which shows a good agreement between numerical and experimental results. The maximum height occurs at t = 1.693 s. As it can be seen, the wave amplitude during the collision is larger than the sum of the amplitudes of the two incident waves, and even though after the collision a slight phase lag is observed, the waves eventually return to their initial shapes.

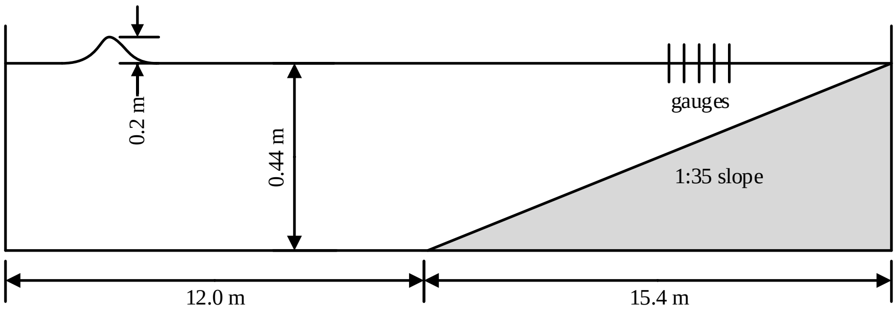

Fig. 10. Experimental setup of Grilli et al. (1994)

4.4 Shoaling of a solitary wave

This test case concerns the nonlinear shoaling of a solitary wave over sloped beaches. The performance of the numerical model is tested with the experimental data of Grilli et al. (1994). The setup consists of a solitary wave of relative amplitude $a/h_0 = 0.2$ propagating in a 27.4 m long flume with constant water depth of $h_0 = 0.44$ m approaching a mild sloped beach (1:35) (Figure 10). The free surface elevation was measured by several wave gauges with locations given in Table 3. The computational grid had a number of 685 cells ($\Delta x = 4$ cm), and the simulation was run for 10 s.

Table 3: Location of the wave gauges in solitary wave shoaling test case

Gauge	g1	g3	g5	g7	g9
Location (m)	21.22	21.92	22.42	22.85	23.84

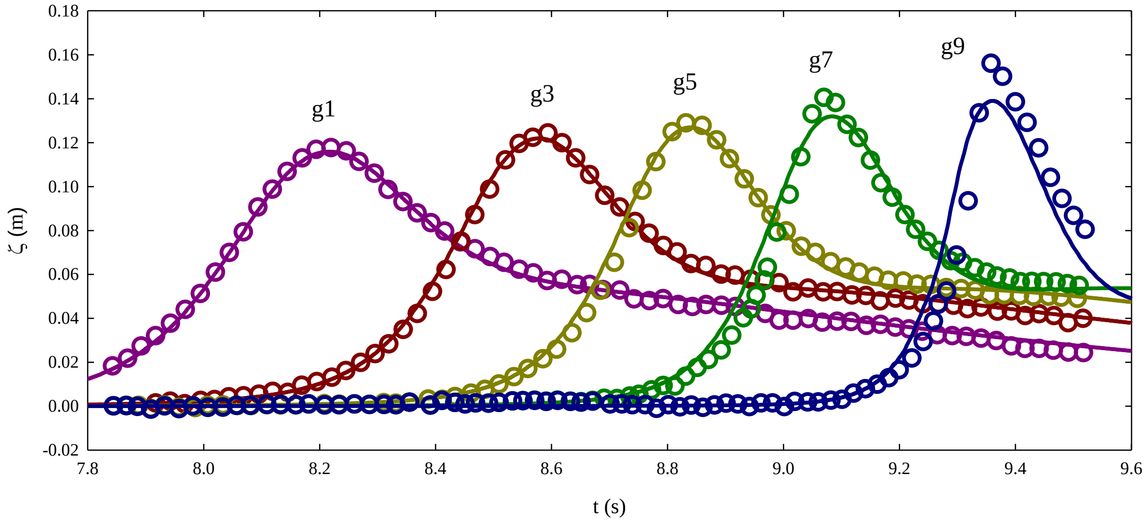

Fig. 11. Comparison of free surface elevations as a function of time between the computed results of present model (lines) and experimental data of Grilli et al. (1994) (circles) at different gauges.

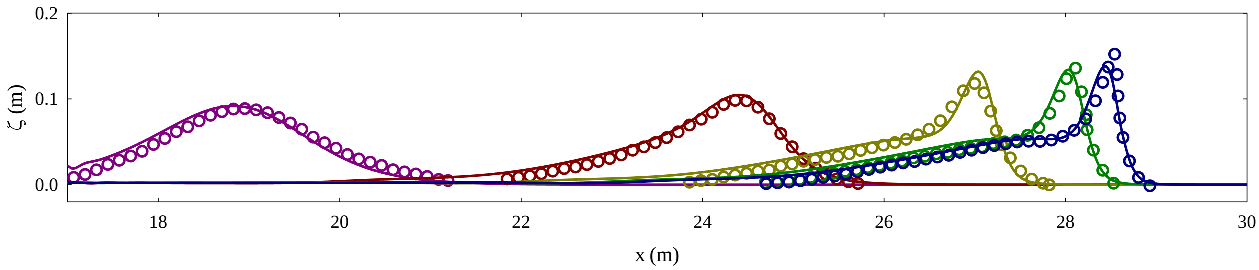

Fig. 12. Comparison of free surface profiles between present model predictions (lines) and experimental data (circles) of Grilli et al. (1994) at times 4.93, 7.28, 9.1, 9.2 and 9.42 s, Left to right

Figure 11 shows the comparison of computed free surface elevations as a function of time against the experimental data of Grilli et al. (1994) at different wave gauges, while in Figure 12 free surface profiles of the computed and experimental results are compared at different times. The results show that with wave propagating toward the slope, it becomes more and more asymmetric and its crest steepens, and by increase of shoaling the wave gets closer to the breaking point. It is observed that the wave evolution is well predicted by the model, with just slight differences close to the breaking point. This shows that the present model is able to describe the shoaling processes with good accuracy.

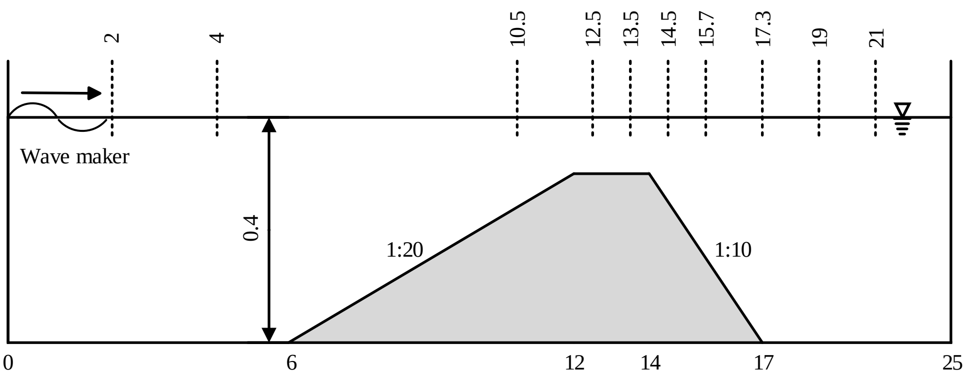

Fig. 13. Periodic waves over a submerged bar: sketch of the basin and gauges location

4.5 Periodic waves over a submerged bar

In this test, the model is examined for a more complex situation involving the propagation of a wave train over a submerged bar following the experimental work of Dingemans (1994) which is a classic test case for investigating both nonlinear and dispersive behavior of the waves. Figure 13 shows the experimental setup of Dingemans (1994). Periodic waves are generated and propagate in a 25 m long flume, with a still water depth of $h_0 = 0.4$ m offshore which reduces to 0.10 m on top of the bar with bottom topography defined as follows (in meters):

$$z(x) = \begin{cases} -0.4 + 0.05(x-6) & 6 \le x \le 12 \\ -0.1 & 12 \le x \le 14 \\ -0.1 - 0.1(x-14) & 14 \le x \le 17 \\ -0.4 & elsewhere \end{cases} \tag{76}$$

Of the experiments reported in Dingemans (1994), we consider the configuration with the relative wave amplitude $a/h_0 = 0.025$ and the period $T = 2.02$ s, which is often used to validate dispersive wave propagation without breaking. Waves are generated using a third-order Stokes solution to impose the free surface elevation governed by:

$$\zeta(x,t) = a\cos\left(2\pi\left(\frac{x}{\lambda} - \frac{t}{T}\right)\right) + \frac{\pi a^2}{\lambda}\cos\left(4\pi\left(\frac{x}{\lambda} - \frac{t}{T}\right)\right) - \frac{\pi^2 a^3}{2\lambda^2}\left[\cos\left(2\pi\left(\frac{x}{\lambda} - \frac{t}{T}\right)\right) - \right. \tag{77}$$

$$\cos\left(6\pi\left(\frac{x}{\lambda}-\frac{t}{T}\right)\right)\Big]$$

where T, a and λ are the wave period, amplitude and wavelength, respectively. The free surface elevation was measured by 10 wave gauges with locations specified in Figure 11. The computational domain is meshed with 625 cells (i.e. $\Delta x = 0.04$ m) and waves are propagated for 35 seconds. Figure 14 shows the time series of computed free surface elevations at different wave gauges, in comparison with the data of Dingemans (1994). Monochromatic waves shoal and steepen over the mild sloped beach, causing transfers of energy toward higher harmonics which are subsequently released in the shallowest part and the lee side of the bar, then continue to propagate at their own deep-water phase speed. In the first 6 gauges, which correspond to the front slope of the bar, the wave shoaling effects are prominent and good agreements could be observed. However, there are discrepancies in the last 4 gauges located on the lee side. These anomalies are most likely because of the high non-linear interactions generated as a result of waves approaching the upper parts of the submerged bar. The same results are reported by Duran and Marche (2015) using finer grid size ($\Delta x = 0.025$ m) and 3rd order polynomials, which suggests that sole improvement in the numerics would not be enough to remove such anomalies. Rather, they seem to result from the one-parameter model, i.e. Eq. (1), deployed here, which is reported to have shortcomings in accurately describing the full release of the “higher harmonics” associated with highly dispersive waves (Duran and Marche 2015).

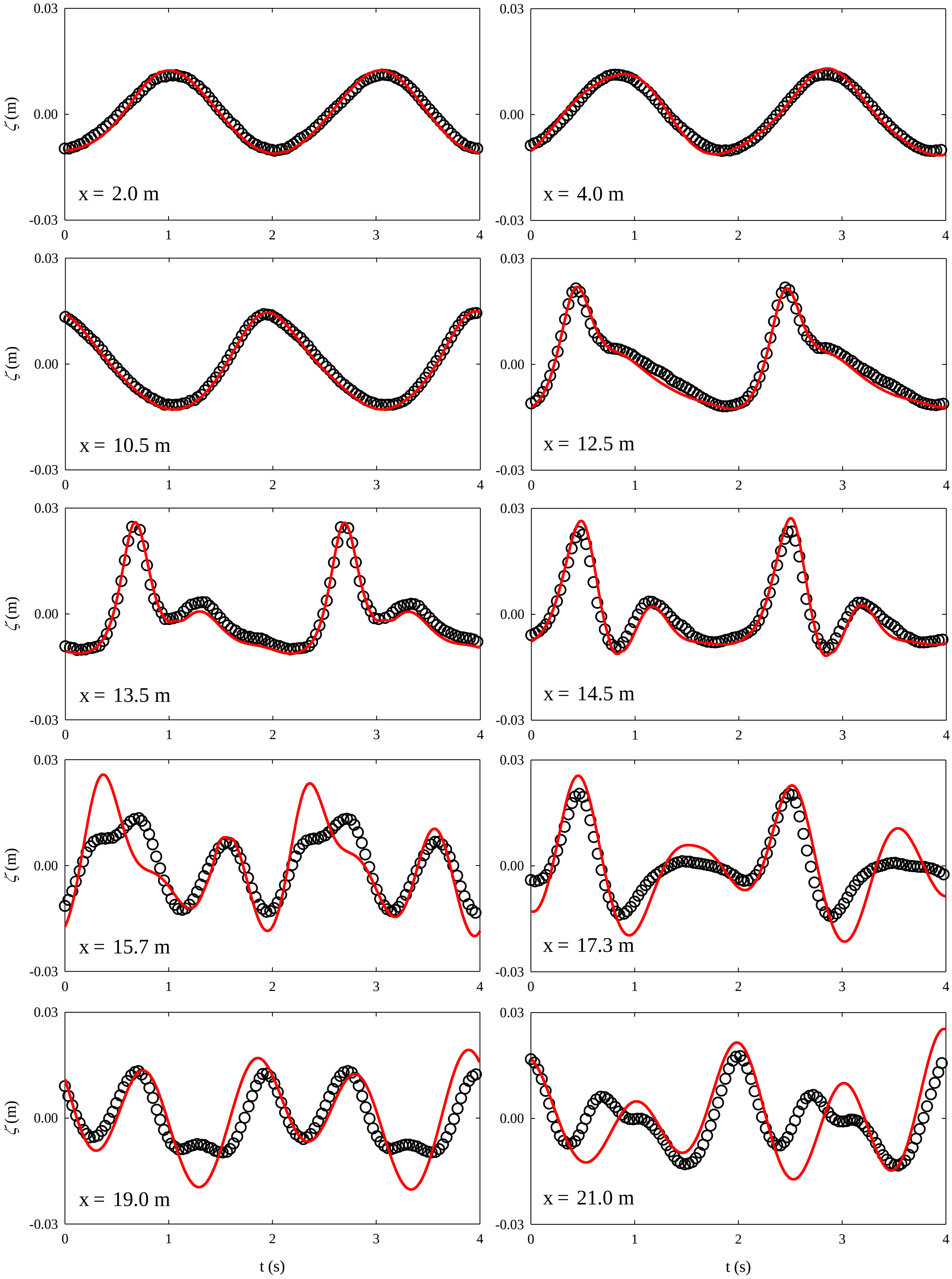

Fig. 14. Time series of free surface elevation of waves passing over the submerged bar at different locations. Comparison between numerical (solid line) and experimental data (circles) of Dingemans (1994)

A possible alternative to improve the simulation for such scenarios would be the three-parameters optimized GN model proposed in Lannes and Marche (2015). However, for general purpose modelling, the latter model is more complex (i.e. to conveniently decompose into a conservative hyperbolic form that also includes elliptic source terms), is 20% more computationally demanding (i.e. it requires the resolution of an additional sparse unsymmetric linear system), and trade-off with sensitivity issues (i.e. to choose and tune across three parameters, instead of one, to achieve a simulation for individual problems).

4.6 Solitary wave breaking and run-up and -down over a sloped beach

This test is considered to assess the ability of the present RKDG2-GN solver to model a high energy wave breaking over a sloped (initially dry) beach with wave run-up and run-down. The domain is a sloping beach (1:19.85) of length 45 m and holding a still water level $h_0 = 1$ m and an incident solitary wave of relative amplitude $a_0/h_0 = 0.28$ (Synolakis, 1987). Simulations are performed on meshes with 300 and 150 cells, respectively. The numerical free surface elevation profiles at different output (normalized) times $t^* = t(g/h_0)^{1/2}$ are included in Figure 15 where they are also compared with the experimental profiles reported in Synolakis (1987), RKDG3-GN results produced in Duran and Marche (2015) using 600 cells, and the results of the non-hydrostatic shallow water model in Lu et al. (2015) solved by a hybrid FV-FD scheme on a mesh with 376 cells. The results show wave height increase due to shoaling until around $t^* = 20$ when breaking occurs. After breaking at $t^* = 23$, the wave height decreases rapidly and the induced run-up collapses over the beach. During $25 \leq t^* \leq 55$, run-up and run-down phases are observed. All the models can be said to be in good agreement with the experiments; however, at the breaking moment ($t^* = 20$) the results of present model and those of Lu et al. (2015)'s model are closer to the experiment. The good performance of the latter could be a result of the higher level of physical complexity in the incorporation of non-hydrostatic terms.

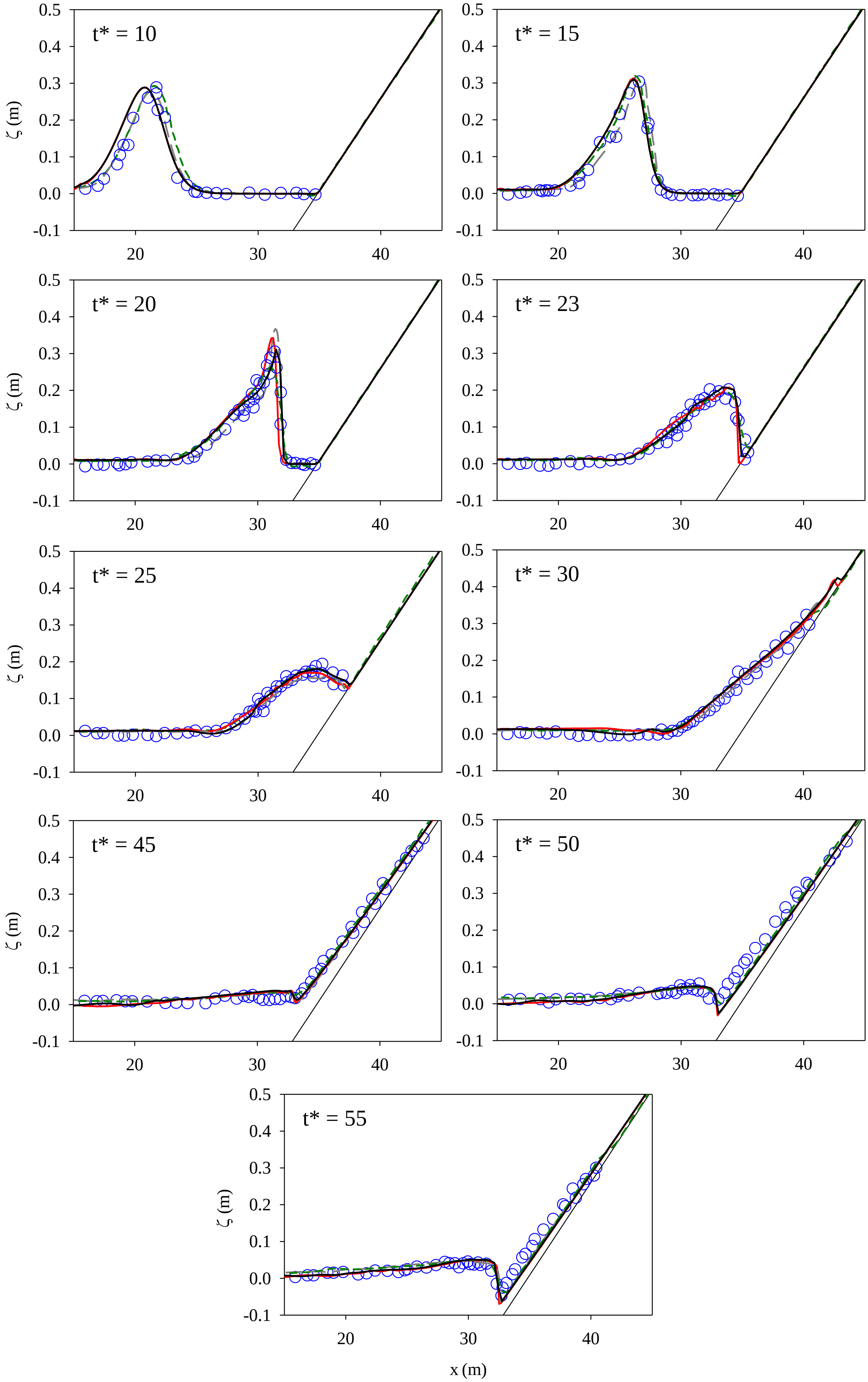

t* = 10
t* = 15
t* = 20
t* = 23
t* = 25
t* = 30
t* = 45
t* = 50
t* = 55
ζ (m)
x (m)

Fig. 15. Comparison of free surface elevation for solitary wave breaking, runup and run down at various instances on a plane beach: experimental data of Synolakis (1987) (circles); numerical results of Lu et al. (2015) using 376 cells (gray long dash); numerical results of Duran and Marche (2015) using 600 cells (green short dash); results of present model with 300 cells (red solid line); results of present model with 150 cells (black solid line). Note that at t*=23, the results of Lu et al. (2015) were not available.

This also shows that using the present numerical criteria (68) for wave breaking detection, despite its simplicity, could well be a convenient choice for the RKDG2-GN model. The higher level of numerical accuracy and of resolution involved in Duran and Marche (2015) model does not seem to comparatively improve much in the predictions. The proposed RKDG2-GN model results on the coarser meshes (i.e. using 150 and 300 cells) remain predominantly close to experimental results throughout the transformations and processes that the wave has undergone, suggesting that it can form the base for an efficient substitute to handle coastal modeling in a fairly affordable model structure.

5. Conclusions

A second-order RKDG method (RKDG2) is proposed to simulate propagation and transformation of fully nonlinear and weakly dispersive waves over domains involving uneven beds and wet-dry fronts. The mathematical model has been based on a set of newly developed efficient 1D Green-Naghdi (GN) equations. The numerical method extends a robust RKDG2 hydrodynamic solver by further considering elliptic source terms that account for dispersive corrections. This has been achieved by a Local Discontinuous Galerkin (LDG) discretization for solving the decoupled elliptic-hyperbolic governing equations and by locally involving fourth-order topography discretization for the dispersive components. Quantitative and qualitative assessments with test cases covering nearshore water flow propagations have been performed. The results demonstrate that the proposed RKDG2-GN solver is able to switch across different water wave patterns, while preserving accuracy, conservation and practical properties featuring the original shallow water RKDG2 model. Future work will further consider strategies for extension and validation for the 2D case, and incorporation of an adaptive meshing strategy.

Acknowledgments

The authors are grateful for two anonymous reviewers for their insightful reviews, which significantly improved the quality of this paper. G. Kesserwani acknowledges the support of the UK Engineering and Physical Sciences Research Council (via grant EP/R007349/1).

References

Agnon, Y., Madsen, P. A., & Schäffer, H. A. (1999). A new approach to high-order Boussinesq models. Journal of Fluid Mechanics, 399, 319-333.

Alvarez-Samaniego, B., & Lannes, D. (2008). Large time existence for 3D water-waves and asymptotics. Inventiones mathematicae, 171(3), 485-541.

Bai, Y., & Cheung, K. F. (2013). Depth-integrated free-surface flow with parameterized non-hydrostatic pressure. International Journal for Numerical Methods in Fluids, 71(4), 403-421.

Barthélemy, E. (2004). Nonlinear shallow water theories for coastal waves. Surveys in Geophysics, 25(3), 315-337.

Bassi, F., & Rebay, S. (1997). A high-order accurate discontinuous finite element method for the numerical solution of the compressible Navier–Stokes equations. Journal of computational physics, 131(2), 267-279.

Beji, S., & Nadaoka, K. (1996). A formal derivation and numerical modelling of the improved Boussinesq equations for varying depth. Ocean Engineering, 23(8), 691-704.

Bonneton, P. (2007). Modelling of periodic wave transformation in the inner surf zone. Ocean Engineering, 34(10), 1459-1471.

Bonneton, P., Chazel, F., Lannes, D., Marche, F., & Tissier, M. (2011). A splitting approach for the fully nonlinear and weakly dispersive Green–Naghdi model. Journal of Computational Physics, 230(4), 1479-1498.

Borthwick, A. G. L., Ford, M., Weston, B. P., Taylor, P. H., & Stansby, P. K. (2006, September). Solitary wave transformation, breaking and run-up at a beach. In Proceedings of the Institution of Civil Engineers-Maritime Engineering (Vol. 159, No. 3, pp. 97-105). Thomas Telford Ltd.

Brocchini, M. (2013, December). A reasoned overview on Boussinesq-type models: the interplay between physics, mathematics and numerics. In Proc. R. Soc. A (Vol. 469, No. 2160, p. 20130496). The Royal Society.

Brocchini, M., & Dodd, N. (2008). Nonlinear shallow water equation modeling for coastal engineering. Journal of waterway, port, coastal, and ocean engineering, 134(2), 104-120.

Caviedes-Voullième, D., & Kesserwani, G. (2015). Benchmarking a multiresolution discontinuous Galerkin shallow water model: Implications for computational hydraulics. Advances in Water Resources, 86, 14-31.

Chen, Q., Kirby, J. T., Dalrymple, R. A., Kennedy, A. B., & Chawla, A. (2000). Boussinesq modeling of wave transformation, breaking, and runup. II: 2D. Journal of Waterway, Port, Coastal, and Ocean Engineering, 126(1), 48-56.

Cienfuegos, R., Barthelemy, E., & Bonneton, P. (2006). A fourth-order compact finite volume scheme for fully nonlinear and weakly dispersive Boussinesq-type equations. Part I: model development and analysis. International Journal for Numerical Methods in Fluids, 51(11), 1217-1253.

Cienfuegos, R., Barthélemy, E., & Bonneton, P. (2009). Wave-breaking model for Boussinesq-type equations including roller effects in the mass conservation equation. Journal of waterway, port, coastal, and ocean engineering, 136(1), 10-26.

Cockburn, B., & Shu, C. W. (1991). The Runge-Kutta local projection P1-discontinuous-Galerkin finite element method for scalar conservation laws. RAIRO-Modélisation mathématique et analyse numérique, 25(3), 337-361.

Cockburn, B., & Shu, C. W. (1998). The local discontinuous Galerkin method for time-dependent convection-diffusion systems. SIAM Journal on Numerical Analysis, 35(6), 2440-2463.

Craig, W., Guyenne, P., Hammack, J., Henderson, D., & Sulem, C. (2006). Solitary water wave interactions. Physics of Fluids, 18(5), 057106.

de Brye, S., Silva, R., & Pedrozo-Acuña, A. (2013). An LDG numerical approach for Boussinesq type modelling. Ocean Engineering, 68, 77-87.

Dingemans, M. W. (1994). Comparison of computations with Boussinesq-like models and laboratory measurements. Deltares (WL).

Dong, H., & Li, M. (2016). A reconstructed central discontinuous Galerkin-finite element method for the fully nonlinear weakly dispersive Green–Naghdi model. Applied Numerical Mathematics, 110, 110-127.

Dumbser, M., & Facchini, M. (2016). A space-time discontinuous Galerkin method for Boussinesq-type equations. Applied Mathematics and Computation, 272, 336-346.

Duran, A. (2014). Numerical simulation of depth-averaged flow models: a class of Finite Volume and discontinuous Galerkin approaches (Doctoral dissertation, Université Montpellier II).

Duran, A., & Marche, F. (2015). Discontinuous-Galerkin discretization of a new class of Green-Naghdi equations. Communications in Computational Physics, 17(03), 721-760.

Duran, A., & Marche, F. (2017). A discontinuous Galerkin method for a new class of Green-Naghdi equations on simplicial unstructured meshes. Applied Mathematical Modelling.

Dutykh, D., Katsaounis, T., & Mitsotakis, D. (2011). Finite volume schemes for dispersive wave propagation and runup. Journal of Computational Physics, 230(8), 3035-3061.

Engsig-Karup, A. P., Hesthaven, J. S., Bingham, H. B., & Madsen, P. A. (2006). Nodal DG-FEM solution of high-order Boussinesq-type equations. Journal of engineering mathematics, 56(3), 351-370.

Engsig-Karup, A. P., Hesthaven, J. S., Bingham, H. B., & Warburton, T. (2008). DG-FEM solution for nonlinear wave-structure interaction using Boussinesq-type equations. Coastal Engineering, 55(3), 197-208.

Eskilsson, C., & Sherwin, S. J. (2003). An hp/spectral element model for efficient long-time integration of Boussinesq-type equations. Coastal Engineering Journal, 45(02), 295-320.

Eskilsson, C., & Sherwin, S. J. (2005). Discontinuous Galerkin spectral/hp element modelling of dispersive shallow water systems. Journal of Scientific Computing, 22(1), 269-288.

Eskilsson, C., & Sherwin, S. J. (2006). Spectral/hp discontinuous Galerkin methods for modelling 2D Boussinesq equations. Journal of Computational Physics, 212(2), 566-589.

Eskilsson, C., Sherwin, S. J., & Bergdahl, L. (2006). An unstructured spectral/hp element model for enhanced Boussinesq-type equations. Coastal Engineering, 53(11), 947-963.

Filippini, A. G., Kazolea, M., & Ricchiuto, M. (2016). A flexible genuinely nonlinear approach for nonlinear wave propagation, breaking and run-up. Journal of Computational Physics, 310, 381-417.

Gassner, G. J., Winters, A. R., & Kopriva, D. A. (2016). A well balanced and entropy conservative discontinuous Galerkin spectral element method for the shallow water equations. Applied Mathematics and Computation, 272, 291-308.

Gobbi, M. F., Kirby, J. T., & Wei, G. E. (2000). A fully nonlinear Boussinesq model for surface waves. Part 2. Extension to O (kh) 4. Journal of Fluid Mechanics, 405, 181-210.

Godunov, S. K. (1959). A difference method for numerical calculation of discontinuous solutions of the equations of hydrodynamics. Matematicheskii Sbornik, 89(3), 271-306.

Green, A. E., & Naghdi, P. M. (1976). A derivation of equations for wave propagation in water of variable depth. Journal of Fluid Mechanics, 78(02), 237-246.

Grilli, S. T., Subramanya, R., Svendsen, I. A., & Veeramony, J. (1994). Shoaling of solitary waves on plane beaches. Journal of Waterway, Port, Coastal, and Ocean Engineering, 120(6), 609-628.

Israwi, S. (2010). Derivation and analysis of a new 2D Green–Naghdi system. Nonlinearity, 23(11), 2889.

Karambas, T. V., & Koutitas, C. (1992). A breaking wave propagation model based on the Boussinesq equations. Coastal Engineering, 18(1-2), 1-19.

Kazolea, M., & Delis, A. I. (2013). A well-balanced shock-capturing hybrid finite volume–finite difference numerical scheme for extended 1D Boussinesq models. Applied Numerical Mathematics, 67, 167-186.

Kennedy, A. B., Chen, Q., Kirby, J. T., & Dalrymple, R. A. (2000). Boussinesq modeling of wave transformation, breaking, and runup. I: 1D. Journal of waterway, port, coastal, and ocean engineering, 126(1), 39-47.

Kesserwani, G. (2013). Topography discretization techniques for Godunov-type shallow water numerical models: a comparative study. Journal of Hydraulic Research, 51(4), 351-367.

Kesserwani, G., & Liang, Q. (2010). A discontinuous Galerkin algorithm for the two-dimensional shallow water equations. Computer Methods in Applied Mechanics and Engineering, 199(49), 3356-3368.

Kesserwani, G., & Liang, Q. (2011). A conservative high-order discontinuous Galerkin method for the shallow water equations with arbitrary topography. International journal for numerical methods in engineering, 86(1), 47-69.

Kesserwani, G., & Wang, Y. (2014). Discontinuous Galerkin flood model formulation: Luxury or necessity?. Water Resources Research, 50(8), 6522-6541.

Kesserwani, G., & Liang, Q. (2012). Locally limited and fully conserved RKDG2 shallow water solutions with wetting and drying. Journal of Scientific Computing, 50(1), 120-144.

Kesserwani, G., Shamkhalchian, A., & Zadeh, M. J. (2014). Fully coupled Discontinuous Galerkin modeling of dam-break flows over movable bed with sediment transport. Journal of Hydraulic Engineering, 140(4), 06014006.

Kirby, R. M., & Karniadakis, G. E. (2005). Selecting the numerical flux in discontinuous Galerkin methods for diffusion problems. Journal of Scientific Computing, 22(1), 385-411.

Kirby, J. T. (2016). Boussinesq models and their application to coastal processes across a wide range of scales. Journal of Waterway, Port, Coastal, and Ocean Engineering, 142(6), 03116005.

Lannes, D., & Marche, F. (2015). A new class of fully nonlinear and weakly dispersive Green–Naghdi models for efficient 2D simulations. Journal of Computational Physics, 282, 238-268.

Le Métayer, O., Gavrilyuk, S., & Hank, S. (2010). A numerical scheme for the Green–Naghdi model. Journal of Computational Physics, 229(6), 2034-2045.

Li, M., Guyenne, P., Li, F., & Xu, L. (2014). High order well-balanced CDG–FE methods for shallow water waves by a Green–Naghdi model. Journal of Computational Physics, 257, 169-192.

Lu, X., Dong, B., Mao, B., & Zhang, X. (2015). A two-dimensional depth-integrated non-hydrostatic numerical model for nearshore wave propagation. Ocean Modelling, 96, 187-202.

Lu, X., & Xie, S. (2016). Conventional versus pre-balanced forms of the shallow-water equations solved using finite-volume method. Ocean Modelling, 101, 113-120.

Lynett, P. J., & Liu, P. L. F. (2004a). Linear analysis of the multi-layer model. Coastal Engineering, 51(5), 439-454.

Lynett, P., & Liu, P. L. F. (2004b). A two-layer approach to wave modelling. In Proceedings of The Royal Society of London A: Mathematical, Physical and Engineering Sciences (Vol. 460, No. 2049, pp. 2637-2669). The Royal Society.

Ma, G., Shi, F., & Kirby, J. T. (2012). Shock-capturing non-hydrostatic model for fully dispersive surface wave processes. Ocean Modelling, 43, 22-35.

Madsen, P. A., & Schäffer, H. A. (1998). Higher–order Boussinesq–type equations for surface gravity waves: derivation and analysis. Philosophical Transactions of the Royal Society of London A: Mathematical, Physical and Engineering Sciences, 356(1749), 3123-3181.

Madsen, P. A., & Sørensen, O. R. (1992). A new form of the Boussinesq equations with improved linear dispersion characteristics. Part 2. A slowly-varying bathymetry. Coastal Engineering, 18(3-4), 183-204.

Madsen, P. A., Bingham, H. B., & Liu, H. (2002). A new Boussinesq method for fully nonlinear waves from shallow to deep water. Journal of Fluid Mechanics, 462, 1-30.

Madsen, P. A., Bingham, H. B., & Schäffer, H. A. (2003, May). Boussinesq-type formulations for fully nonlinear and extremely dispersive water waves: derivation and analysis. In Proceedings of the Royal Society of London A: Mathematical, Physical and Engineering Sciences (Vol. 459, No. 2033, pp. 1075-1104). The Royal Society.

Madsen, P. A., Murray, R., & Sørensen, O. R. (1991). A new form of the Boussinesq equations with improved linear dispersion characteristics. Coastal Engineering, 15(4), 371-388.

Murillo, J., García-Navarro, P., & Burguete, J. (2009). Time step restrictions for well-balanced shallow water solutions in non-zero velocity steady states. International journal for numerical methods in fluids, 60(12), 1351-1377.

Nwogu, O. (1993). Alternative form of Boussinesq equations for nearshore wave propagation. Journal of waterway, port, coastal, and ocean engineering, 119(6), 618-638.

Orszaghova, J., Borthwick, A. G., & Taylor, P. H. (2012). From the paddle to the beach–A Boussinesq shallow water numerical wave tank based on Madsen and Sørensen's equations. Journal of Computational Physics, 231(2), 328-344.

Panda, N., Dawson, C., Zhang, Y., Kennedy, A. B., Westerink, J. J., & Donahue, A. S. (2014). Discontinuous Galerkin methods for solving Boussinesq–Green–Naghdi equations in resolving non-linear and dispersive surface water waves. Journal of Computational Physics, 273, 572-588.

Peregrine, D. H. (1967). Long waves on a beach. Journal of fluid mechanics, 27(04), 815-827.

Roeber, V., & Cheung, K. F. (2012). Boussinesq-type model for energetic breaking waves in fringing reef environments. Coastal Engineering, 70, 1-20.

Roeber, V., Cheung, K. F., & Kobayashi, M. H. (2010). Shock-capturing Boussinesq-type model for nearshore wave processes. Coastal Engineering, 57(4), 407-423.

Sampson, J. J. (2009). A numerical solution for moving boundary shallow water flow above parabolic bottom topography. ANZIAM Journal, 50, 898-911.

Schäffer, H. A., & Madsen, P. A. (1995). Further enhancements of Boussinesq-type equations. Coastal Engineering, 26(1-2), 1-14.

Serre, F. (1953). Contribution à l'étude des écoulements permanents et variables dans les canaux. La Houille Blanche, (6), 830-872.

Shi, F., Kirby, J. T., Harris, J. C., Geiman, J. D., & Grilli, S. T. (2012). A high-order adaptive time-stepping TVD solver for Boussinesq modeling of breaking waves and coastal inundation. Ocean Modelling, 43, 36-51.

Sørensen, O. R., Schäffer, H. A., & Madsen, P. A. (1998). Surf zone dynamics simulated by a Boussinesq type model. III. Wave-induced horizontal nearshore circulations. Coastal Engineering, 33(2), 155-176.

Su, C. H., & Gardner, C. S. (1969). Korteweg-de Vries Equation and Generalizations. III. Derivation of the Korteweg-de Vries Equation and Burgers Equation. Journal of Mathematical Physics, 10(3), 536-539.

Steinmoeller, D. T., Stastna, M., & Lamb, K. G. (2012). Fourier pseudospectral methods for 2D Boussinesq-type equations. Ocean Modelling, 52, 76-89.

Steinmoeller, D. T., Stastna, M., & Lamb, K. G. (2016). Discontinuous Galerkin methods for dispersive shallow water models in closed basins: Spurious eddies and their removal using curved boundary methods. Ocean Modelling, 107, 112-124.

Synolakis, C. E. (1987). The runup of solitary waves. Journal of Fluid Mechanics, 185, 523-545.

Tavelli, M., & Dumbser, M. (2014). A high order semi-implicit discontinuous Galerkin method for the two dimensional shallow water equations on staggered unstructured meshes. Applied Mathematics and Computation, 234, 623-644.

Tissier, M., Bonneton, P., Marche, F., Chazel, F., & Lannes, D. (2012). A new approach to handle wave breaking in fully non-linear Boussinesq models. Coastal Engineering, 67, 54-66.

Tonelli, M., & Petti, M. (2009). Hybrid finite volume–finite difference scheme for 2DH improved Boussinesq equations. Coastal Engineering, 56(5), 609-620.

Tonelli, M., & Petti, M. (2010). Finite volume scheme for the solution of 2D extended Boussinesq equations in the surf zone. Ocean Engineering, 37(7), 567-582.

Toro, E. F., & Garcia-Navarro, P. (2007). Godunov-type methods for free-surface shallow flows: A review. Journal of Hydraulic Research, 45(6), 736-751.

Walkley, M. A. (1999). A numerical method for extended Boussinesq shallow-water wave equations (Doctoral dissertation, University of Leeds).

Wei, Z., & Jia, Y. (2013). A depth-integrated non-hydrostatic finite element model for wave propagation. International Journal for Numerical Methods in Fluids, 73(11), 976-1000.

Wei, G., & Kirby, J. T. (1995). Time-dependent numerical code for extended Boussinesq equations. Journal of Waterway, Port, Coastal, and Ocean Engineering, 121(5), 251-261.

Wei, G., Kirby, J. T., Grilli, S. T., & Subramanya, R. (1995). A fully nonlinear Boussinesq model for surface waves. Part 1. Highly nonlinear unsteady waves. Journal of Fluid Mechanics, 294(13), 71-92.

Xing, Y. (2014). Exactly well-balanced discontinuous Galerkin methods for the shallow water equations with moving water equilibrium. Journal of Computational Physics, 257, 536-553.

Yamazaki, Y., Kowalik, Z., & Cheung, K. F. (2009). Depth-integrated, non-hydrostatic model for wave breaking and run-up. International journal for numerical methods in fluids, 61(5), 473-497.

Zelt, J. A. (1991). The run-up of nonbreaking and breaking solitary waves. Coastal Engineering, 15(3), 205-246.

Zijlema, M., & Stelling, G. S. (2008). Efficient computation of surf zone waves using the nonlinear shallow water equations with non-hydrostatic pressure. Coastal Engineering, 55(10), 780-790.